Check for updates

Strategies for the preparation of high-performance inorganic mixed-halide perovskite solar cells

Xin Liu, [ID] * Jie Li, [ID] Xumei Cui, Xiao Wang* and Dingyu Yang [ID] *

Inorganic halide perovskites have attracted significant attention in the field of photovoltaics (PV) in recent years due to their superior intrinsic thermal stability and excellent theoretical power conversion efficiency (PCE). $CsPbI_3$ with a bandgap of ~1.7 eV is considered to be the most potential candidate for PV application. However, bulk $CsPbI_3$ films exhibit poor phase stability. The substitution of some iodide ions with bromide/chloride in $CsPbI_3$ results in the formation of mixed-halide $CsPbX_3$ perovskites, which exhibit a good balance between phase stability and efficiency. The halogen-tunable mixed-halide inorganic perovskites have a bandgap matching the sunlight region and show great potential for application in multi-junction tandem and semitransparent solar cells. Herein, the progress of mixed-halide $CsPbX_3$ PSCs is systematically reviewed, including $CsPbI_xBr_yCl_{3-x-y}$- and $CsPbIBr_2$-based IPSCs. In the case of $CsPbIBr_2$ IPSCs, we introduce the low-temperature deposition of $CsPbIBr_2$ films, doping methods for the preparation of high-quality $CsPbIBr_2$ films and strategies for improving the performance of solar cells. Furthermore, the mechanism of crystallization/interface engineering for the preparation of high-quality $CsPbIBr_2$ films and efficient solar cells devices is emphasized. Finally, the development direction of further improving the PV performance and commercialization of mixed-halide IPSCs are summarized and prospected.

1 Introduction

Halide perovskites have received increasing attention in the past few years as bright new stars in optoelectronic devices. In the case of thin-film photovoltaic (PV) devices, halide perovskite materials exhibit excellent photophysical properties such as

a, College of Optoelectronic Engineering, Chengdu University of Information Technology, Chengdu 610225, China. E-mail: liuxin@cuit.edu.cn; wangxiao@cuit.edu.cn; yangdingyu@cuit.edu.cn

Xin Liu is an Assistant Professor with the College of Optoelectronic Engineering, Chengdu University of Information Technology. She received her B.S. Degree from Hefei University of Technology in 2011 and PhD from South China University of Technology in 2016. From 2016 to 2017, she joined high-tech companies in China for research on organic light-emitting diodes. From 2017 to 2019, she was a Post-Doctoral Fellow with the University of Electronic Science and Technology of China. She joined Chengdu University of Information Technology in 2020 as an Assistant Professor. Her research interests include inorganic/organic semiconductor materials, thin-film photovoltaic devices and device physics.

Xiao Wang is an Assistant Professor with the College of Optoelectronic Engineering, Chengdu University of Information Technology. She received her B.S. Degree in 2012 and PhD in 2018 from the University of Electronic Science and Technology of China. During 2016–2018, she worked as a Visiting Scholar at the Centre for Organic Photonics & Electronics (COPE) at The University of Queensland. From June 2019 to June 2020, she was a Post-Doctoral Fellow at COPE. She joined Chengdu University of Information Technology in 2021 as an Assistant Professor. Her research interests include semiconductor and device physics, organic photovoltaics, and perovskite solar cells.
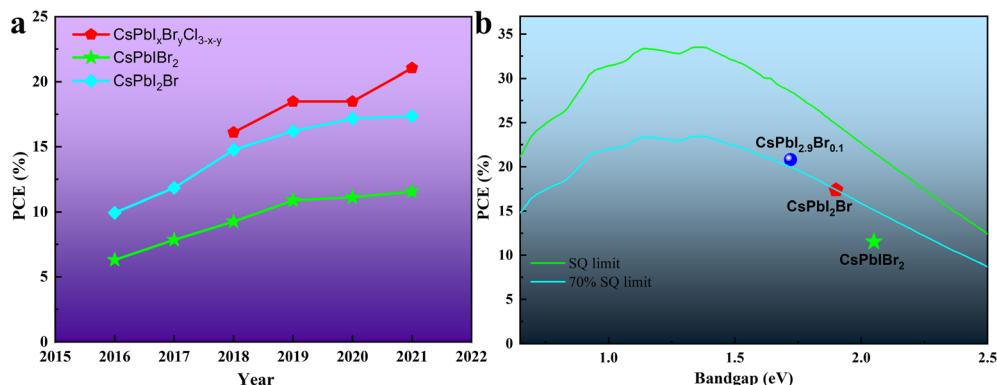
Fig. 1 (a). Champion PCE of IPSCs with time. The devices are divided into 3 groups by changing the halogen compositions. (b). Champion PCE of different IPSCs compared with the SQ limit.

high extinction coefficient/carrier mobility, long carrier diffusion length, high defect tolerance, small exciton binding energy and tunable bandgaps.[1–7] Strikingly, since Miyasaka *et al.* first adopted the halide perovskite material as a light absorber in a PV device and reported a power conversion efficiency (PCE) of 3.8% in 2009,[8] organic–inorganic hybrid perovskite solar cells (OIH-PSCs) have obtained a PCE of more than 25%,[9–16] which is comparable to that of the silicon-based solar cells currently dominating the PV field. The general chemical formula of organic–inorganic hybrid perovskite (OIHP) materials is ABX_3, where A is a monovalent organic cation (methylammonium $(CH_3NH_3^+$ and MA^+), formamidinium $(HC(NH_2)_2^+$ and FA^+) or their mixture), B is a divalent cation $(Pb^{2+}$ and $Sn^{2+})$ and X is a halogen ion $(I^-$, Br^-, and Cl^- or their mixture). However, due to the presence of volatile organic components, *i.e.*, MA^+ or FA^+, OIH-PSCs undergo some compositional and structural degradation under persistent attack from heat, humidity, oxygen and light.[17–23] Thus, to realize the commercialization of perovskite PV devices, the instability issues of OIH-PSCs have attracted great attention.[24–26]

Inorganic cesium (Cs^+) ions completely occupy the A-sites in the general chemical formula of ABX_3, forming inorganic cesium lead halide perovskite materials $(CsPbX_3)$. Due to the

lack of volatile and hygroscopic organic cations, these materials show robust resistance to high temperature and moisture.[27–30] In 2015, Hodes's group revealed that organic components are not essential components to achieve efficient inorganic perovskite solar cells (IPSCs).[31] They also demonstrated that the $CsPbBr_3$ perovskite material has better thermal stability than organic–inorganic hybrid $MAPbBr_3$ perovskite, and the $CsPbBr_3$-based PV devices exhibit better thermal stability.[32] In 2016, the PCE of mixed-halide IPSCs based on the first $CsPbBr_2$ and the first $CsPbI_2Br$ was 4.7%[33] and close to 10%,[34] respectively. Since then, the efficiency and stability of IPSCs have been rapidly improved by referring to the research experience of OIH-PSCs and the exploration of inorganic perovskite, as illustrated in Fig. 1a. However, compared with the Shockley–Queisser (SQ) efficiency limits and the requirements of practical PV applications,[35,36] there is still much room to improve the efficiency and long-term stability of IPSCs (Fig. 1b).

At present, the commonly used light absorption layers in IPSCs include $CsPbBr_3$, $CsPbIBr_2$, $CsPbI_2Br$ and $CsPbI_3$. $CsPbI_3$ with a bandgap (E_g) of about 1.7 eV is considered the most potential candidate for PV application. Unfortunately, bulk $CsPbI_3$ exhibits poor phase stability, which rapidly converts to a non-perovskite orthorhombic phase $(E_g = 2.82$ eV).[37–40] The large bandgap of $CsPbBr_3$ $(E_g = 2.25$ eV) limits the light collection, consequently reducing the device efficiency.[41,42] Alternatively, the substitution of some of iodide ions with bromide/chloride ions in $CsPbI_3$ to form mixed-halide $CsPbX_3$ perovskites can provide a good balance between phase stability and efficiency. Mixed-halide inorganic perovskites such as $CsPbIBr_2$ have attracted significant attention due to their increased Goldschmidt's tolerance factor t, thus stabilizing the black phase by partially substituting I^- with the smaller Br^-. Furthermore, cubic-phase $CsPbIBr_2$ and $CsPbI_2Br$ perovskites show great potential in multi-junction tandem and semi-transparent solar cells owing to their suitable optical bandgap of 2.05 eV[43] and 1.92 eV,[44] respectively. Importantly, mixed-halide inorganic perovskites can remain as a photoactive black phase at room temperature (RT), but inevitably convert to a non-perovskite phase when exposed to a humid environment. This phase transformation process is reversible when heated to

Dingyu Yang is a Professor with the College of Optoelectronic Engineering, Chengdu University of Information Technology. He received his B.S. and M.S. Degree from Lanzhou University in 2000 and 2003, respectively, and PhD from Sichuan University in 2009. From October 2012 to February 2013, he worked as a Visiting Scholar at Nanyang Technological University. He joined Chengdu University of Information Technology in 2003. His research interests include optoelectronic detection technology and new energy technology.

Fig. 2 Summary and strategies for the preparation of high-performance mixed-halide CsPbX$_3$ IPSCs.

350 °C in a dry environment.[45] To overcome the problems of environmental instability and achieve high-performance IPSCs, composition engineering and interface engineering play very important roles. For instance, Li$^+$ doping can improve the optical, morphological and electronic properties of CsPbIBr$_2$ films. Doping Mn^{2+} or Sn^{2+} in CsPbIBr$_2$ can narrow its bandgap and enlarge its light response region. The introduction of the smaller F$^-$ in the X-site of CsPbI$_2$Br can induce the formation of an α/δ-phase heterojunction, which facilitates efficient exciton dissociation and charge transport. Interfacial strategies between the perovskite film and the ETL or HTL can provide more suitable energy level alignments and passivate defects, and then effectively suppress the interfacial recombination.

In this review, as outlined in Fig. 2, we systematically summarize the reported mixed-halide CsPbX$_3$ IPSCs. Firstly, the recent progress on the replacement of non-halogen or halogen anions in CsPbX$_3$ IPSCs will be introduced. Then, we discuss and analyze the progress on CsPbIBr$_2$-IPSCs. The section on CsPbIBr$_2$-IPSCs covers the preparation of CsPbIBr$_2$ films at low temperature, doping methods for the fabrication of high-quality CsPbIBr$_2$ films and strategies for improving the PV performance of solar cells. The effective methods for the preparation of high-quality CsPbIBr$_2$ films and the mechanism of crystallization/interface engineering for high-performance solar cells devices are emphasized. Finally, we present a summary and prospect on promising directions for further promoting the PV performance and realizing the commercialization of mixed-halide CsPbX$_3$ solar cells.

2 Basic properties of CsPbX$_3$ perovskites

2.1 Crystal structure

Regarding crystal-based thin film optoelectronic devices, it is important to deeply understand their crystal structure to obtain high-performance halide perovskite PV devices with long-term stability. Halide perovskites are generally represented by the chemical formula ABX$_3$, where the monovalent cation A-site such as MA$^+$, FA$^+$, and Cs$^+$ occupies the corner positions (0, 0, 0), the bivalent cation B-site such as Pb^{2+}, Sn^{2+}, and Ge^{2+} is located at the central positions (1/2, 1/2, 1/2), and the anion X such as I$^-$, Br$^-$ and Cl$^-$ is located at the center of the six planes

(1/2, 1/2, 0), forming the crystal structure of three-dimensional (3D) perovskites with corner-sharing BX$_6$ octahedra (Fig. 3a). According to the environmental conditions, CsPbX$_3$ inorganic perovskite can form 4 types of crystal structures including cubic phase (α-, Pm3m), tetragonal phase (β-, P4/mbm), orthorhombic phase (γ-, Pbnm), and non-perovskite orthorhombic phase (δ-, Pnma).[46] The optoelectronic properties and crystal stability of the CsPbX$_3$ perovskite are significantly influenced by the different tilting angles of the PbX$_6$ octahedra, and therefore the type of CsPbX$_3$ perovskite phase is closely related to its PV properties and device long-term stability.

The formation and geometric stability of the crystal structure of ABX$_3$ compounds can be empirically determined using Goldschmidt's tolerance factor (t) and the octahedral factor (μ), which allow researchers to pre-screen the formation of suitable components of a stable perovskite lattice. To maintain the perovskite cubic crystal structure, t: $t = (R_A + R_X)/\sqrt{2}(R_B + R_X)$ (ref. 47 and 48) and $\mu(R_B/R_X)$ (ref. 49) should be satisfied in the range of 0.9 to 1 and 0.4 to 0.9,[50] where R_A, R_B, and R_X are the ionic radii of the corresponding cation and anion, respectively. The BX$_6$ framework can only contain certain ions to achieve the geometric stability of halide perovskites. A t factor below 0.9 leads to a distorted perovskite structure due to the tilting of the PbX$_6$ octahedra. A t factor between 0.9 and 1.0 leads to the formation of symmetric cubic-phase perovskite. When t is greater than 1, a hexagonal structure with a face-sharing octahedron is formed. Meanwhile, with a t factor at the required lower or upper limit, a too small or large A cation generally leads to a non-perovskite phase. The μ assesses whether the B atoms will tend to octahedral coordination of the X atoms. When it is greater than 0.4, a stable BX$_6$ octahedron can be formed. Thus, because the requirements of t and μ must be satisfied simultaneously, only a limited number of combinations of A, B, and X ion types can form 3D perovskites.

Cs$^+$ has been identified as the preferred inorganic ion to substitute the organic MA$^+$/FA$^+$ in the perovskite structure. In the case of CsPbX$_3$ perovskite compounds, Cs$^+$ completely occupies the A-site. The photoactive black phase of CsPbI$_3$ perovskite is easily converted to the undesirable yellow δ-CsPbI$_3$ at room temperature (RT) due to the small ionic radius of Cs$^+$, which makes it difficult to support the [PbI$_6$]$^{4-}$ octahedron. The partial replacement of I$^-$ by Br$^-$ can reduce the size of the Cs-X
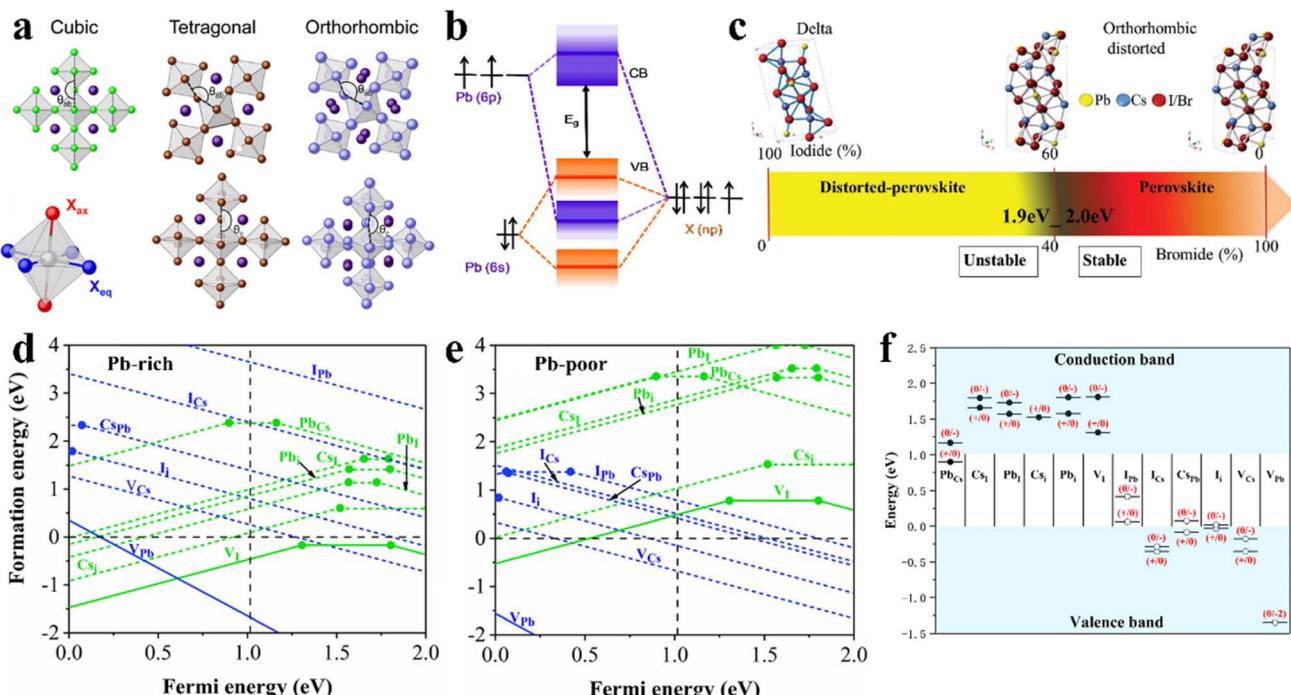
Fig. 3 (a). Polyhedron models of crystal structures of cubic, tetragonal, and orthorhombic. Reprint with permission.[67] Copyright 2018, the American Chemical Society. (b). Schematic representation of bonding/antibonding orbitals of APbX$_3$ exhibiting the formation of the VB and CB. Reproduced with permission.[52] Copyright 2016, the American Chemical Society. (c). CsPbX$_3$ crystal structures as a function of the iodine/bromine ratio. Reproduced with permission.[61] Copyright 2018, Wiley-VCH. Calculated defect formation energy as a function of the Fermi energy E_F of Pb-rich (d) and Pb-poor (e) films of cubic CsPbI$_3$. (f). Intrinsic point defect transition energy levels in cubic CsPbI$_3$. (d–f) Reproduced with permission.[65] Copyright 2017, the American Institute of Physics.

coordination polyhedron, enabling Cs$^+$ to retain the [PbX$_6$]$^{4-}$ octahedron structure, and then adjust the values of t and μ to a more desirable range.[51] Due to the partial replacement of I$^-$ with the smaller Br$^-$, mixed-halogen inorganic perovskites such as CsPbI$_2$Br and CsPbIBr$_2$ exhibit excellent stability, and thus have attracted much attention. Furthermore, the bandgaps of the cubic-phase CsPbI$_2$Br and CsPbIBr$_2$ perovskites are 1.92 eV[44] and 2.05 eV,[43] respectively, showing great potential in tandem and semitransparent solar cells. More importantly, the mixed-halogen CsPbX$_3$ perovskites can maintain a photoactive black phase at RT, but inevitably transform to a non-perovskite phase when exposed to a humid environment. Given that the distortion degree of the [PbI$_6$]$^{4-}$ octahedron will seriously influence the transition between different phases, its distortion degree can be controlled by introducing steric hindrance or external disturbances, which will help CsPbX$_3$ to remain in the desired black phase.

2.2 Optoelectronic properties of CsPbX$_3$ perovskites

The excellent optical and electrical properties of semiconductor perovskites greatly depend on the nature of their electronic structures. For typical CsPbX$_3$ perovskites, their conduction band minimum (CBM) is composed of a combination of lead 6p orbital and halogen np orbitals with the main contribution from Pb 6p (Fig. 3b), while their valence band maximum (VBM) mainly consists of mixed lead 6s orbitals and halogen np orbitals with the dominant contribution from X np.[52] The

contribution of the element to each band strongly depends on the perovskite stoichiometry. It is well known that the high efficiency of PSCs is related to direct their bandgap transition, high absorption coefficient, *etc.*, while the optical absorption of perovskite materials is related to their electronic band structure.

To gain deeper insight into the relationships between the structure and perovskite PV performance, theoretical investigations are conducive to acquiring a comprehensive understanding of CsPbX$_3$ perovskites and serve as a guidance to accurately design and develop new component materials with advanced optoelectronic properties. Adopting PbI$_2$ as an initial structural model, polymorphs of alkali metal lead halide perovskites with the cubic structure have been studied, indicating that while the Pb^{2+} 6s lone-pairs are stereochemically inert, the presence of proximal instabilities can have implications in the functional properties of these materials.[53] Thus, the excitation and recombination of electrons and excitons are confined to the octahedron, similar to the widely studied OIHPs.[54,55] According to density functional theory (DFT) and considering relativistic corrections and spin–orbit interactions, the electronic structures of cubic-phase CsPbCl$_3$, CsPbBr$_3$, and CsPbI$_3$ perovskites have been calculated.[56] It is evident that the energy band structures of CsPbX$_3$ perovskites are not affected by their halide composition apart from the difference in their bandgap values, and thus all the CsPbX$_3$ perovskites exhibit direct bandgaps, demonstrating numerous potential applications in the field of optoelectronics.[57–60]

Table 1 Summary of the PV performance of non-halogen or mixed-halogen ion-based CsPbX$_3$ IPSCs

Device architecture	Deposition method	Active area (cm^2)	PCE (%)	J_{sc} (mA cm^{-2})	V_{oc} (V)	FF (%)	Stability	Year (ref.)
FTO/c-TiO$_2$/CsPbI$_{2.85}$Br$_{0.15}$ (@210 °C)/Spiro-OMeTAD/Au	One-step spin-coating	0.09	18.43	20.64	1.09	82.3	—	2021 (ref. 78)
ITO/ZnO/CsPbI$_{2.4}$Br$_{0.6}$ (@275 °C)/Spiro-OMeTAD/Au	One-step spin-coating	—	18.14	18.16	1.22	82.07	—	2021 (ref. 79)
FTO/c-TiO$_2$/CsPbI$_{2.33}$Br$_{0.67}$ (@190 °C)/carbon	One-step spin-coating	0.07	12.40	17.30	1.01	70.98	Retained 84% of initial efficiency after stored in ambient environment with RH 15–20% for 200 h	2021 (ref. 80)
ITO/P3CT-N/CsPbI$_{2.8}$Br$_{0.2}$ (@180 °C)/PCBM/Ag	One-step spin-coating	0.09	13.14	18.78	1.00	70.0	Maintained 80% of the initial PCE value exposed to an atmosphere with RH in the range of 40–60% for 6 h	2022 (ref. 92)
ITO/ZnO/CsPbI$_{2.4}$Br$_{0.6}$:Cl/Spiro-OMeTAD/Au	One-step spin-coating	0.0475	17.14	17.57	1.21	80.36	—	2021 (ref. 83)
FTO/c-TiO$_2$/CsPbI$_{2.85}$Br$_{0.149}$Cl$_{0.001}$ (@210 °C)/Spiro-OMeTAD/Au	One-step spin-coating	0.09	19.65	19.94	1.23	80.11	Maintained 91.2% of initial PCE value for over 30 days (RH 15–30%, at 10 °C)	2021 (ref. 84)
FTO/SnO$_2$/CsPbI$_{2.5}$Br$_{0.5}$ (@350 °C)/Spiro-OMeTAD/MoO$_3$/Au	One-step spin-coating	0.05	17.10	17.67	1.30	74.18	Maintained 85% of initial PCE exposed to N$_2$ atmosphere after 1500 h under continuous light illumination	2020 (ref. 85)
FTO/SnO$_2$/CsPb(I$_{0.75}$Br$_{0.25}$)$_3$-0.5FAOAc (@280 °C)/Spiro-OMeTAD/Au	One-step spin-coating	0.16	17.0	15.9	1.34	79.6	—	2020 (ref. 86)
FTO/c-TiO$_2$/CsPbI$_{2.84}$Br$_{0.16}$-0.1CsTa (@180 °C)/Spiro-OMeTAD/Au	One-step spin-coating	0.09	16.59	19.48	1.10	77.30	Maintained 87.41% of the initial PCE after 500 h of storage under 80% RH at 80 °C	2021 (ref. 87)
FTO/c-TiO$_2$/CsPbI$_{3-x}$Br$_x$ (@210 °C)/HA/Spiro-OMeTAD/Au	One-step spin-coating	0.09	20.8	20.55	1.233	81.9	—	2021 (ref. 88)
ITO/SnO$_2$/CsPbI$_{1.8}$Br$_{1.2}$ (@160 °C)/TACl/PBDB-T/MoO$_3$/Au/ZnO/PFN/PM6:Y6/MoO$_3$/Al	One-step spin-coating	0.0988	21.04	13.36	2.05	76.82	Retained 94% of initial PCE after 120 h of UV-light irradiation	2022 (ref. 89)
FTO/SnO$_2$/ZnO/CsPbI$_{1.5}$Br$_{1.5}$ (@200 °C)/Spiro-OMeTAD/Au	One-step spin-coating	0.06	14.05	14.1	1.29	77.1	—	2021 (ref. 91)
FTO/TiO$_2$/CsPbI$_2$Br:1.0% Co(Ac)$_2$ (@50 °C/@150 °C/@270 °C)/Spiro-OMeTAD/Ag/Au	One-step spin-coating (Ac$^-$ doped)	—	15.04	15.43	1.21	80.46	Retained 76% of initial PCE for over 50 days storage in N$_2$ glovebox	2020 (ref. 93)
ITO/SnO$_2$/5% Pb(Ac)$_2$:CsPbI$_2$Br (@280 °C)/PTAA/Au	One-step ultrasonic spray (Ac$^-$ doped)	0.09	10.06	13.99	1.12	65	Retained 76% of the initial efficiency stored in N$_2$ glovebox at 85 °C	2021 (ref. 70)
FTO/c-TiO$_2$/5% Pb(Ac)$_2$:CsPbI$_2$Br (@350 °C)/Spiro-OMeTAD/Ag	One-step spin-coating (Ac$^-$ doped)	0.07	12	13.98	1.17	74	Maintained ≈80% PCE after 30 days storage at T ≈ 20 °C and RH ≈ 20%	2018 (ref. 94)
FTO/TiO$_2$/4.5% Pb(Ac)$_2$:CsPbI$_2$Br (@35 °C/@120 °C/@165 °C)/Spiro-OMeTAD/Au	One-step spin-coating (Ac$^-$ doped)	0.09	15.56	15.28	1.30	78.51	Maintained 98% of initial PCE for 14 days storage in air (25 °C and 30% humidity)	2019 (ref. 69)
ITO/SnO$_2$/1% CsCl:CsPbI$_2$Br (@45 °C/@110 °C/@180 °C)/Spiro-OMeTAD/Au	One-step spin-coating (Cl$^-$ doped)	0.1	11.04	12.87	1.33	64	Retained ~80% of initial PCE after 360 h exposure in ambient air with RH ~65%	2021 (ref. 95)
FTO/c-TiO$_2$/0.015 M Pb(DDTC)$_2$:CsPbI$_2$Br (@43 °C/@160 °C)/P3HT/Au	One-step spin-coating (DDTC$^-$ doped)	0.0625	17.03	15.78	1.34	80.52	Maintained > 98% of original PCE in ambient conditions with RH = 15 ± 3% for 1440 h	2020 (ref. 96)

Table 1 (*Contd.*)

Device architecture	Deposition method	Active area (cm²)	PCE (%)	J_{sc} (mA cm^{-2})	V_{oc} (V)	FF (%)	Stability	Year (ref.)
FTO/c-TiO$_2$/m-TiO$_2$/CsPbBrI$_{1.78}$F$_{0.22}$ (@150 °C)/Spiro-OMeTAD/Ag	One-step spin-coating (F$^-$ doped)	—	10.26	14.94	1.01	68	Retained 69.81% of the initial PCE after 10 days storage under 20% RH at RT	2018 (ref. 68)
FTO/c-TiO$_2$/m-TiO$_2$/4-GBACl:CsPbI$_2$Br (@50 °C/@160 °C)/Spiro-OMeTAD/Ag	One-step spin-coating (Pb-X framework)	0.09	15.59	15.42	1.28	79	Maintained 88% of initial PCE after 1200 h aging at 25 °C and 20% RH under ambient conditions	2021 (ref. 97)
FTO/c-TiO$_2$/CsGA$_{0.04}$PbTh$_3$Ac$_{0.02}$ (@210 °C)/Spiro-OMeTAD/Au	One-step spin-coating (GCA passivation)	0.09	19.37	20.14	1.17	82.1	Retained 80% of initial PCE value after being stored for one month under ambient conditions without encapsulation	2022 (ref. 81)
ITO/SnO$_2$/β-CsPbI$_{2.85}$(BrCl)$_{0.15}$/PTB7-th BHJ (@210 °C)/Spiro-OMeTAD/Au	One-step spin-coating (DMAI-mediated)	0.0832	19.0	20.7	1.12	81.8	Maintained over 90% of the initial PCE after being stored in N$_2$ glovebox for 6 months exposed to light illumination for 144 h	2022 (ref. 82)

A continuous change in halide composition from I to Br to Cl leads to systematic changes in the optical bandgap of halide perovskites (Fig. 3c).[61] It is worth noting that the Urbach parameter (E_u), which is a measure of the sub-bandgap tail absorption and associated with static disorder in semiconductors, is abnormally low for halide perovskites. Most importantly, the optical absorption coefficients (α) of Pb-based halide perovskites are quite high and their absorption onsets are very sharp, indicating that only a very thin film can absorb all photons above their bandgap.

In CsPbX$_3$ perovskites, data on the diffusion lengths and their related parameters (carriers mobilities and lifetimes) are limited. Obviously, perovskite films obtained under different conditions show different charge carrier lifetimes. Using the time-resolved microwave conductivity technique, Hutter *et al.* reported that the charge carrier lifetimes exceeded 10 μs in vapor-deposited CsPbI$_3$, while the carrier lifetimes of spin-coated black-phase CsPbI$_3$ films were less than 0.2 μs.[62] For the same CsPbI$_3$ perovskite fabricated by solution deposition, the lifetime of the film was over 20 ns.[63] In addition, the lifetime value was around 14 ns for a solution-deposited CsPbI$_2$Br film.[64] Values of 2–7 μs were reported for CsPbBr$_3$ macroscopic single crystals.

Given that defects can significantly change the electronic properties of perovskite materials, thus affecting the performance of PSCs, it is imperative to have a deep understanding of the defect characteristics to obtain efficient PV devices. In an ideal crystal structure, each atom is located in a specific position. However, due to the defective lattice arrangement at extended distances or the addition of foreign atoms, perovskite polycrystalline films grown and post-processed by solution processes at low temperature will inevitably have some defects.

The crystallographic defects in CsPbX$_3$ show at least three types of different point defects. Fig. 3d and e show the formation energies of CsPbX$_3$ intrinsic point defects calculated in Pb-rich and Pb-poor films.[65,66] There are three types of intrinsic point defects, as follows: (1) vacancies (atoms missing in the lattice: V$_{Cs}$, V$_{Pb}$, and V$_I$), (2) interstitials (atoms occupying the space between atoms in the lattice: Cs$_i$, Pb$_i$, and I$_i$), and (3) anti-site substitutions (atoms occupying the wrong site in the lattice: Cs$_{Pb}$, Cs$_I$, Pb$_{Cs}$, Pb$_I$, I$_{Cs}$, and I$_{Pb}$), where A$_B$ means that A is replaced by B. According to the energy sites of the point defects in the bandgap, they can be divided into shallow and deep-level states. The activation energy of shallow-level defects is lower, while deep-level defects are far away from the CBM and VBM and close to the center of the bandgap, as shown in Fig. 3f.[65] Shallow defects, such as V$_{Cs}$, V$_I$, V$_{Pb}$, Cs$_i$, I$_i$, and Cs$_{Pb}$, have a low formation energy, while deep defects, such as Pb$_I$, Pb$_i$, I$_{Pb}$, and I$_{Cs}$, have a high formation energy. Electrons or holes are captured by deep defect states and are difficult to detrap.

3 CsPbX$_3$ (X: non-halogen or halogen mixed ions)-based IPSCs

Vacuum thermal deposition is mature technology used in industry at present, which can easily prepare multilayer films in

large areas, and the resultant films have good uniformity. However, the vacuum deposition method requires precise control of the stoichiometric ratios of the precursor, and it is usually difficult to control the crystal structure. Thus, the solution-processed methods are usually adapted to prepare $CsPbX_3$ perovskite films owing to their simple preparation and low energy cost, especially given that most perovskite films only require low-temperature annealing. Generally, perovskite deposition can be divided into two solution processing methods, *i.e.*, one-step and two-step sequential deposition. In a two-step process, PbX_2 is first deposited on the substrate, and then coated with CsX, allowing the two precursors to react to form a $CsPbX_3$ film. In a typical one-step process, the perovskite film is directly deposited from a solution containing all the precursors.

The replacement of non-halogen or halogen anions in the X-site is an effective strategy to improve the structure stability of

inorganic $CsPbX_3$ perovskite. Thus far, halogen ions of Cl^- and F^- and non-halogen ions of Ac^- and SCN^- have been used to dope $CsPbX_3$ to finely tune its crystal structure and phase stability. For example, Fu *et al.* introduced F^- into the X-site of $CsPbI_2Br$ to adjust its phase heterostructure and t.[68] It was proven that incorporating the smaller F^- could induce the formation of an α/δ-phase heterojunction, which is beneficial for the efficient dissociation of excitons and charge transport. In another study, Ac^- doping in the $CsPbI_2Br$ perovskite produced multiple benefits including lower trap densities, longer carrier lifetime, and fast charge transportation, thus resulting in a PCE of 15.56% and ultrahigh V_{oc} of 1.30 V for $CsPbI_{2-x}Br(Ac)_x$-based IPSCs.[69] Recently, using the one-step ultrasonic spray deposition method, Liu's group prepared Ac^--doped $CsPbI_2Br$ perovskite.[70] Combining the vacuum extraction during processing, they obtained a $CsPbI_2Br$ film with improved quality, full coverage and long carrier lifetime. Also, a PCE of 10.06% was
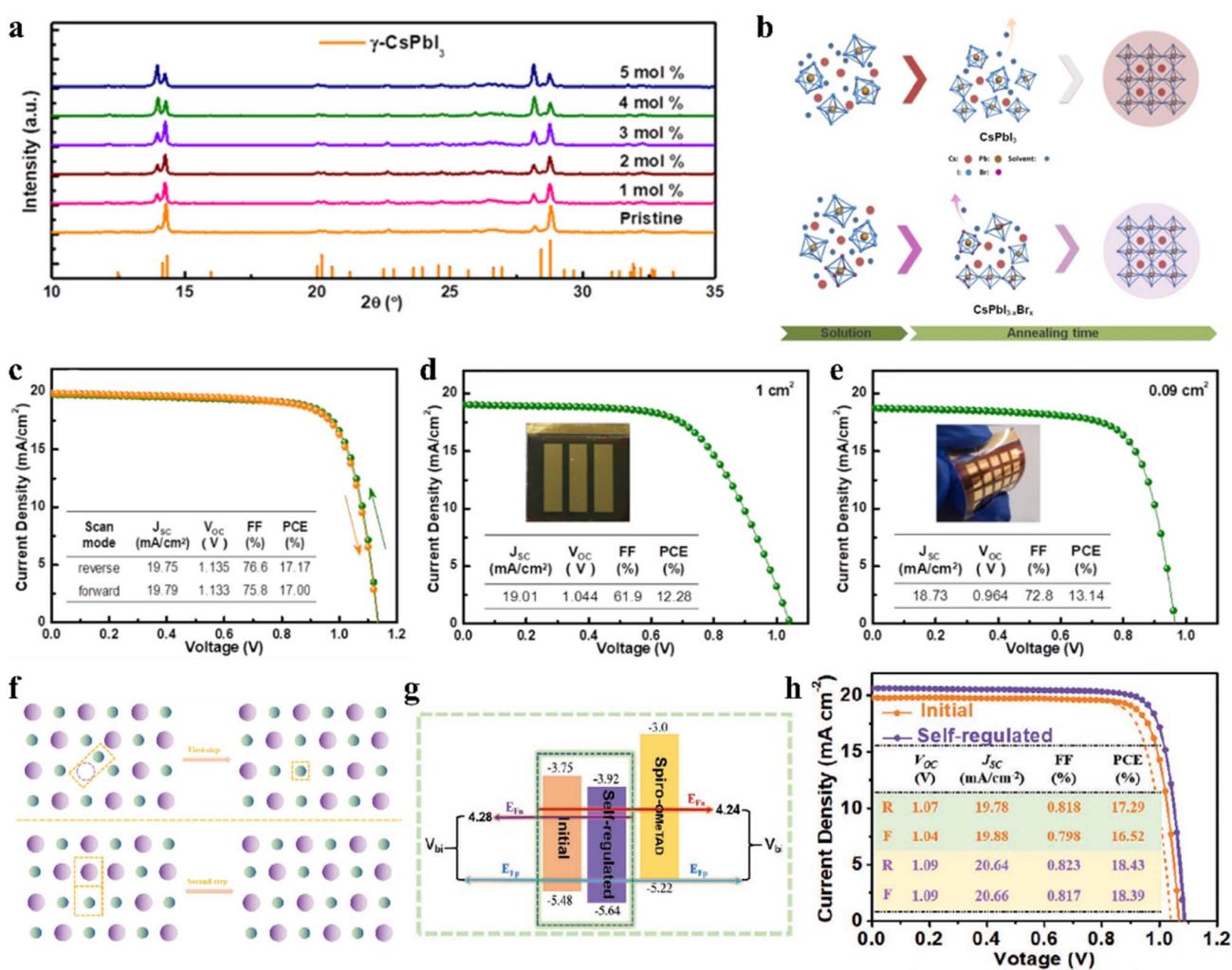

Fig. 4 (a). XRD patterns of γ-$CsPbI_3$:Cl_x films. Reproduced with permission.[72] Copyright 2019, Elsevier. (b). Schematic diagram for Br-driven crystalline grain growth. $J-V$ characteristics (c) under both the reverse and forward scan directions with an active area of 0.09 cm^2; (d) on a glass substrate with an area of 1 cm^2; and (e) on a PET/ITO/TiO$_2$ substrate with an area of 0.09 cm^2. (b–e) Reprinted with permission.[76] Copyright 2019, the American Chemical Society. (f). Proposed schematic diagram of defect-regulation processes. (g). Schematic illustration of energy levels and V_{bi}. (h). $J-V$ characteristics measured in the forward and reverse directions under AM1.5G illumination. (f–h) Reproduced with permission.[78] Copyright 2021, Wiley-VCH.

obtained for n–i–p IPSCs with good thermal stability due to the reduced defect density and nonradiative recombination loss. Table 1 summarizes the PV performance of non-halogen or mixed-halogen ion-based $CsPbX_3$ IPSCs.

3.1 $CsPbI_xCl_{3-x}$-based IPSCs

The regulation of the halide component by introducing Br and Cl has been proven to be a feasible route to improve the stability of IPSCs. For example, appropriate Cl doping in $CsPbX_3$ can improve the stability of the black phase.[71–73] Surface Cl-doped $CsPbI_3$ IPSCs with PTACl passivation treatment exhibited a PCE of 19.03% with high stability.[73] Dastidar *et al.* co-deposited colloidal NCs of pure $CsPbCl_3$ and $CsPbI_3$ to ensure high Cl doping levels and nanometer-scale mixed film, which exhibited improved stability in humid conditions compared to the undoped state.[71] In another study, a stable black-phase γ-$CsPbI_3$ was fabricated by doping Cl ions (Fig. 4a), in which the incorporation of Cl decreased the trap density and improved the electron and hole mobilities.[72] Consequently, the Cl-treated γ-$CsPbI_3$ IPSCs yielded a PCE as high as 16.07% and exhibited slight degradation after continuous light soaking or long-term exposure in dry air. A small amount of lead chloride ($PbCl_2$) additive was introduced in the $CsPbI_{3-x}Br_x$ perovskite precursor

to suppress the recombination in the perovskite film.[74] Consequently, $CsPbI_{3-x}Br_x$ IPSCs with a bandgap of 1.77 eV exhibited an exciting PCE of 18.64% and V_{oc} as high as 1.25 V with the V_{oc} loss as low as 0.52 V, which showed excellent photostability with less than 6% efficiency drop under continuous 1 sun equivalent illumination over 1000 h.

3.2 $CsPbI_yBr_{3-y}$-based IPSCs

The incorporation of small amount of Br can also adjust the t, while the mixing of I/Br can improve the stability of the $CsPbI_3$ perovskite.[75] By incorporating 5% Br ions in $CsPbI_3$ (Fig. 4b), the mixed-halide $CsPbI_{2.85}Br_{0.15}$ IPSCs achieved a PCE of 17.17% and stabilized PCE of 16.83% with low E_{loss} of 0.58 eV and delivered a PCE of 12.28% and 13.14% for large areas (1 cm^2) and flexible substrates, as shown in Fig. 4c–e, respectively.[76] $CsPb_{0.4}Sn_{0.6}I_{2.4}Br_{0.6}$ perovskite with a narrow bandgap of 1.35 eV was developed and the corresponding IPSCs exhibited a PCE of 12.34%.[77] The defect concentration of aged $CsPbI_{3-x}$-Br_x polycrystalline films was about 2-orders of magnitude lower than that of the freshly synthesized films due to the self-digested anti-site defect pairs, in which the origin of the defect annihilation is intimately associated with the strain in the $CsPbI_{3-x}Br_x$ film (Fig. 4f and g).[78] The assembled
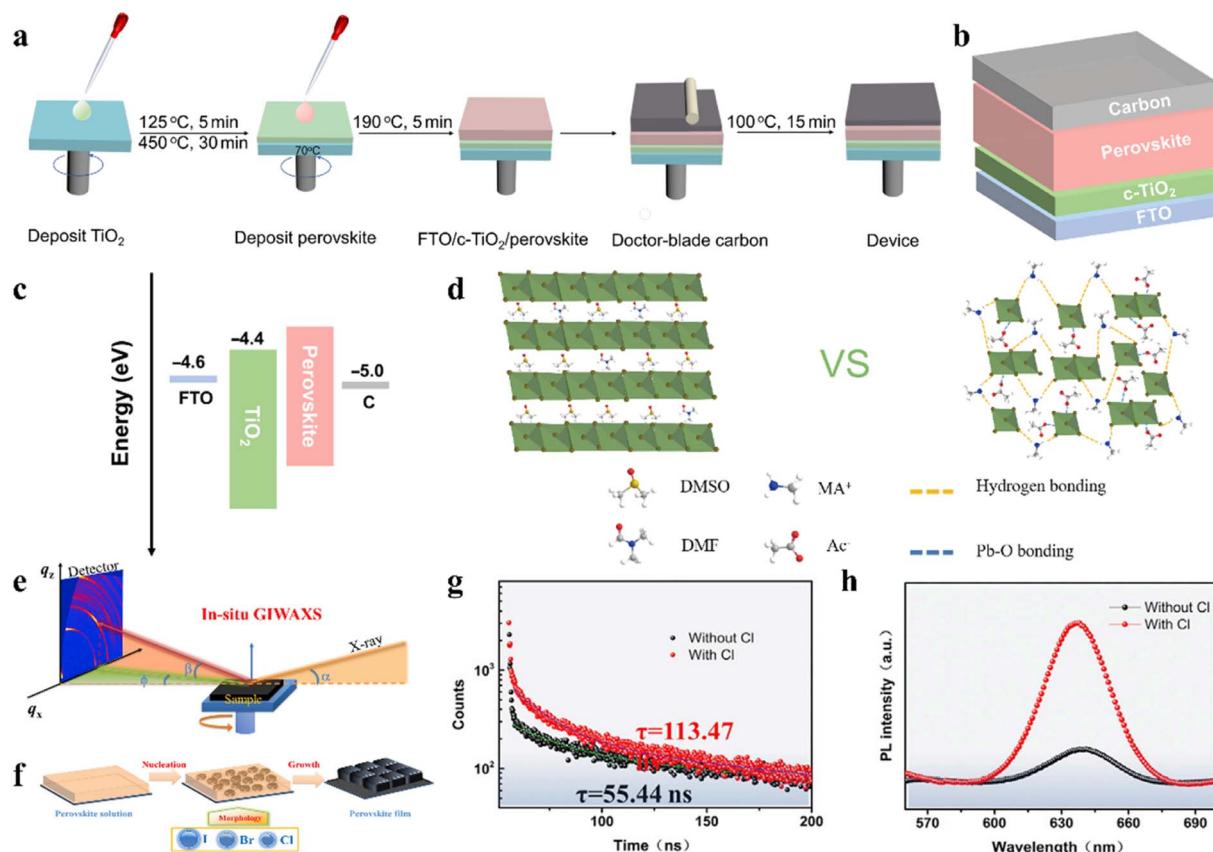

Fig. 5 (a). Schematic illustration of device fabrication process. (b). Device configuration of HTM-free carbon-based IPSCs. (c). Energy level diagram of IPSCs. (a–c) Reproduced with permission.[80] Copyright 2021, Wiley-VCH. (d). Schematic illustration of interaction in the precursor solutions. Reproduced with permission.[85] Copyright 2020, Wiley-VCH. (e). Schematic of *in situ* GIWAXS characterization. (f). Schematic of perovskite film-formation procedures. (g). TRPL decay curves. h. Steady-state PL. (e–h) Reproduced with permission.[83] Copyright 2021, Elsevier.

$CsPbI_{3-x}Br_x$ IPSCs acquired a PCE of 18.43% after self-regulation treatment, which was higher than that of the device with the fresh film (17.29%), as illustrated in Fig. 4h. Meanwhile, the hysteresis was suppressed owing to the reduced strain.

Currently, Wu *et al.* systematically studied the working mechanism of the light soaking (LS) effect in $CsPb(I_{1-x}Br_x)_3$ IPSCs.[79] They found that LS can promote the migration of halogen ions, effectively giving rise to defect passivation. Based on these understandings, a PCE of 18.14% for $CsPb(I_{0.8}Br_{0.2})_3$ IPSCs was achieved by fine-tuning the amount of excessive PbI_2 in the precursor. Composition engineering strategy was proposed to achieve high-quality perovskite films with a large grain size of over 1 μm and fabricate carbon-based IPSCs by incorporating a certain amount of bromide in the $CsPbI_3$ perovskite (Fig. 5a).[80] It was found that the incorporation of bromide induced a high-quality intermediate phase and contributed to the formation of a smooth perovskite film, thus leading to a longer carrier lifetime and lower band edge disorder. Finally, carbon electrode-based $CsPbI_{2.33}Br_{0.67}$ IPSCs (Fig. 5b and c) exhibited a PCE of 12.40% and retained 84% of their initial value after storage for 200 h in the ambient environment (RH 15–20%).

3.3 $CsPbI_xBr_yCl_{3-x-y}$-based IPSCs

Several studies have demonstrated that the phase stability of $CsPbX_3$ perovskites can be effectively improved by combining different halogens.[81,82] To investigate the influence of ternary mixed-halides on the film crystallization mechanism and phase evolution of inorganic perovskite $CsPbX_3$ (X = I, Br, Cl) under spin-coating, Ma *et al.* adopted the state-of-art *in situ* grazing-incidence wide-angle X-ray scattering (GIWAXS) technique, as shown in Fig. 5e.[83] They found that the Br component not only can regulate the crystallization kinetics and affect the formation of the film, but also promote the photoactive phase formation and suppress the unwanted yellow phase transition, as shown by the mechanism presented in Fig. 5f. Moreover, the introduction of Cl can improve the crystallinity and orientational order of the bulk film, which helps to prolong the charge carrier lifetime and suppress the non-radiative recombination (Fig. 5g and h). Hence, with the assistance of Cl doping, the optimized composition $CsPb(I_{0.8}Br_{0.2})_3$:Cl IPSCs obtained a record high PCE of 17.14% with the small V_{oc} E_{loss} of 0.6 eV. Another example reported a PCE of 19.65% with V_{oc} of 1.23 V, corresponding to E_{loss} of 0.48 eV for triple halide-mixed $CsPb(I_{2.85}Br_{0.149}Cl_{0.001})$ IPSCs deposited in the ambient atmosphere using an *in situ* hot oxygen cleansing strategy.[84] It was found that the hot oxygen treatment not only effectively removed the organic residues, but also passivated the halogens vacancies to reduce the trap states and non-radiative recombination losses in the perovskite layer.

The coordination interaction of the precursor solution plays a key role in regulating the crystallization of perovskites. For example, an effective interaction tailoring strategy was developed for the $CsPbI_{3-x}Br_x$ perovskite by adopting the ionic liquid solvent MAAc.[85] The results showed that oxygen with lone pair electrons (C=O) on Ac^- had strong interaction with Pb^{2+} and the N–H⋯I hydrogen bonds, which enabled the formation of a stable perovskite precursor solution and allowed the high-
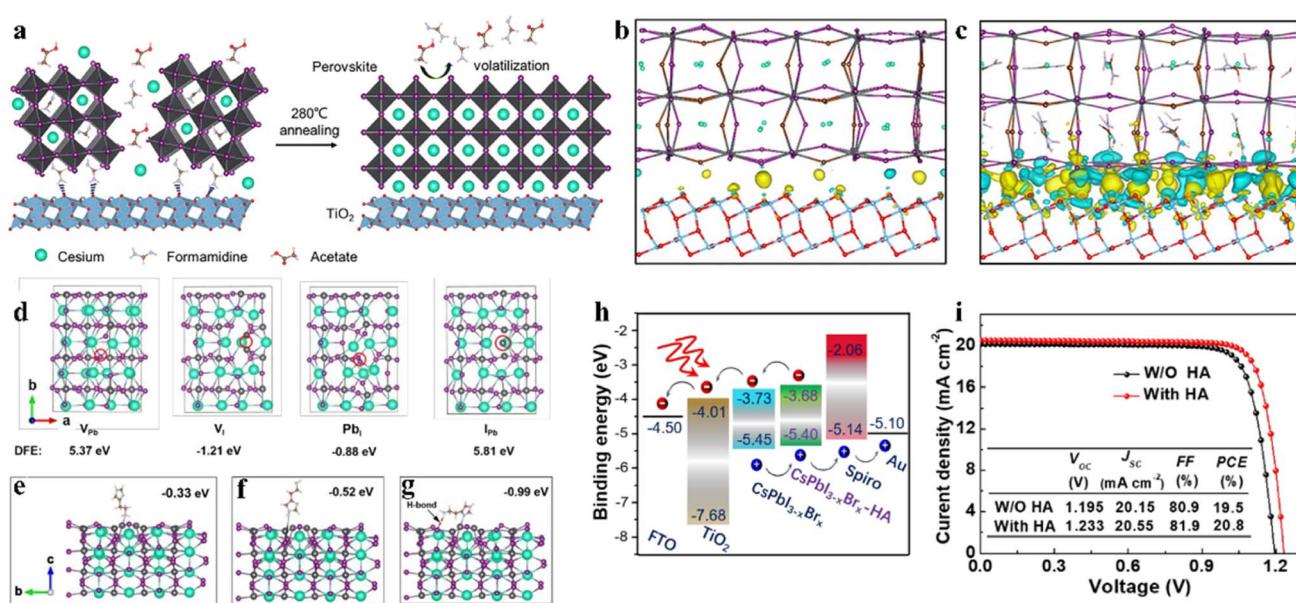

Fig. 6 (a). Schematic illustration of the IPE process. The real-space distribution of difference charge density at the interfaces for (b) $CsPb(I_{0.75}Br_{0.25})_3$/$TiO_2$ and (c) $Cs_{0.5}FA_{0.5}Pb(I_{0.75}Br_{0.25})_3$/$TiO_2$. (a–c) Reproduced with permission.[86] Copyright 2020, Elsevier. (d). Top view of the four types of surface defects and the corresponding DFT. Theoretical models of perovskite with molecular surface interaction of V_I with HA: (e) –NH_2 with V_I; (f) imidazole ring with V_I; (g) synergetic effect of both –NH_2 and imidazole with V_I. (h). Energy diagram of a complete IPSC passivated by HA. (i). $J–V$ curves of the devices with and without HA passivation measured at 100 mW cm^{-2} irradiation in the reverse scan direction. (d–i) Reproduced with permission.[88] Copyright 2021, Wiley-VCH.

quality production of pinhole-free, large grain size, flat inorganic perovskite films by retarding the crystallization (Fig. 5d). By controlling the ratio of I and Br, a series of IPSCs with a one-step, without the necessity for anti-solvent treatment, air-processing approach regardless of humidity, showed a PCE of 13.82% ($CsPbI_{1.5}Br_{1.5}$), 15.82% ($CsPbI_2Br$), and 17.10% ($CsPbI_{2.5}Br_{0.5}$), respectively.

An intermediate-phase engineering strategy was developed to obtain robust interfacial contact by utilizing volatile organic salts, as shown by the mechanism in Fig. 6a.[86] The introduction of organic cations doped in the perovskite lattice led to the formation of an organic–inorganic hybrid perovskite intermediate phase in the initial film and promoted high-quality interfacial contact through hydrogen bonding (Fig. 6b and c). In addition, $CsPbI_{2.84}Br_{0.16}$ films with small grain sizes were achieved by utilizing cesium trimethylacetate (CsTa) organic salt as an additive, in which the large steric hindrance effects of the Ta^- anions efficiently prevented the tilt of the $[PbI_6]^{4-}$

octahedra to inhibit the phase transition process from the corner-shared perovskite to the edge-shared non-perovskite structure.[87] Furthermore, the Ta^- groups firmly bonded onto the surface of the $CsPbI_{2.84}Br_{0.16}$ crystal at the X-site and increased the energy barrier for X-site vacancy generation (from 0.816 eV to 1.217 eV). Finally, the 0.1-CsTa $HPbI_3$-prepared IPSCs exhibited a PCE of 16.59% and retained 80.88% of their initial efficiency after more than 1200 h in air (relative humidity (RH): 20%).

Interfacial modification has been proven to be an effective method for improving the perovskite phase stability, passivating defects and enhancing the performance of IPSCs. According to their DFT investigation, Gu *et al.* disclosed that the iodine vacancies (V_I) on the surface of $CsPbI_{3-x}Br_x$ perovskite films were the predominant defects trapping free charge carriers.[88] To intentionally passivate V_I in the perovskite films and prohibit the nonradiative recombination in devices, the histamine (HA) molecule was adopted, which could effectively
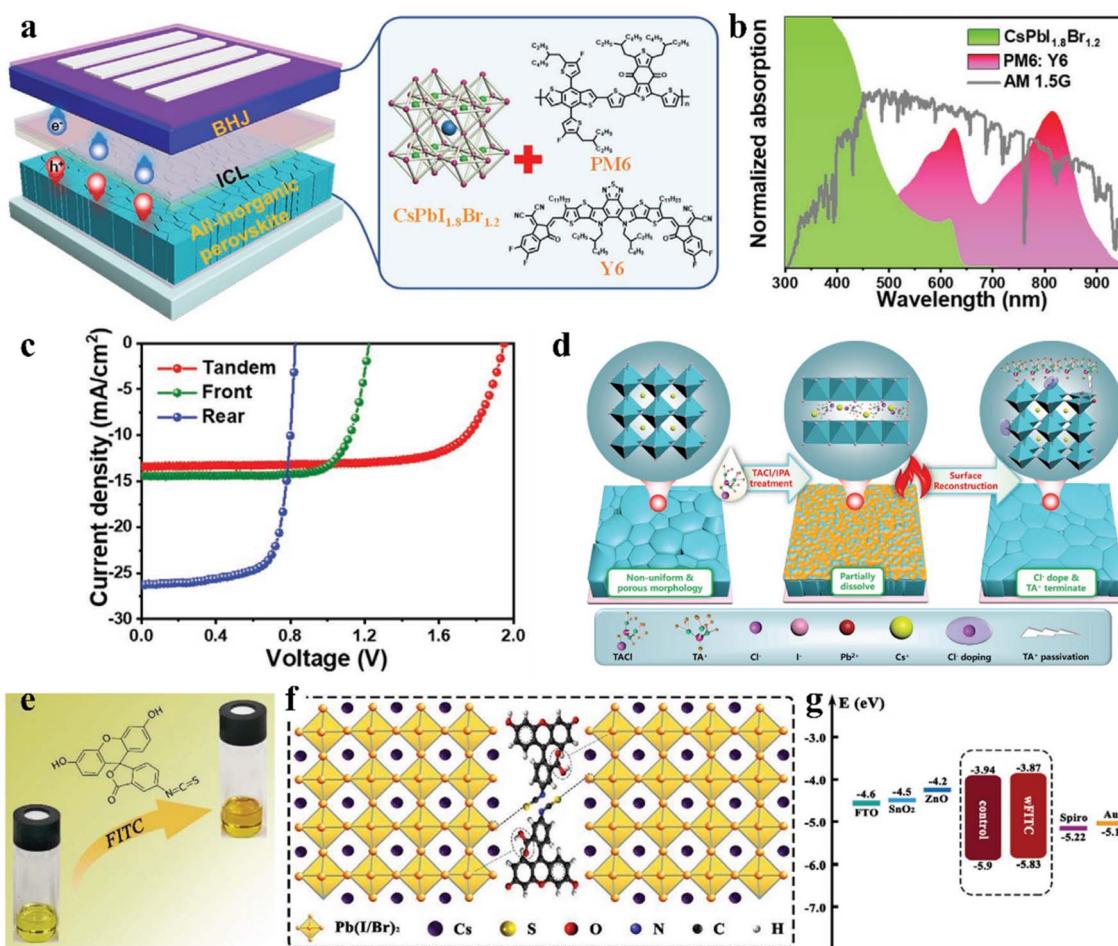

Fig. 7 (a). Left: device structure of all-inorganic perovskite/organic 2T TSC. Right: crystal structure of front all-inorganic perovskite $CsPbI_{1.8}Br_{1.2}$ and the molecular structures of the donor and acceptor materials in the rear cell. (b). Normalized absorption spectra of $CsPbI_{1.8}Br_{1.2}$ and PM6:Y6 films and the AM1.5G spectrum. (c). *J–V* curves of 2T TSC, front and rear solar cells under AM1.5G 100 mW cm^{-2} illumination. (d). Schematic illustration of the TACl and IPA synergistically induced SR processes. (a–d) Reproduced with permission.[89] Copyright 2022, Wiley-VCH. (e). Pristine perovskite solution (left) and perovskite/FITC hybrid solution (right). (f). Schematic illustration of the interaction between FITC and perovskite. (g). Energy level diagram constructed from UV-vis and UPS measurements. (e–g) Reproduced with permission.[91] Copyright 2021, Wiley-VCH.

interact with V_I on the surface of the perovskite film *via* synergetic effects from both Lewis-base-acid reaction and hydrogen bond formation, and thus significantly reduced the number of uncoordinated Pb^{2+} and Pb clusters, as the mechanism illustrated in Fig. 6d–g. Moreover, the energy level position was also regulated to facilitate hole transfer at the heterojunction contact between the perovskite and HTL, as shown in Fig. 6h. Consequently, by optimizing the concentration of HA, the $CsPbI_{3-x}Br_x$ IPSCs delivered an outstanding PCE of 20.8% (Fig. 6i) and stabilized value of 20.4%, corresponding to 72% of the SQ efficiency limit. Recently, a surface reconstruction (SR) strategy was developed by post-treating a $CsPbI_{1.8}Br_{1.2}$ film with the organic ammonium halide salt trimethylammonium chloride (TACl) to reduce the surface defect states (Fig. 7d).[89] The repaired $CsPbI_{1.8}Br_{1.2}$ surface effectively inhibited nonradiative recombination and promoted hole transport, providing efficient charge recombination in the interconnecting layer in the two-terminal tandem SCs (2T-TSCs) (Fig. 7a and b). Consequently, the $CsPbI_{1.8}Br_{1.2}$ perovskite/organic 2T-TSCs yielded a PCE of 21.04% with an ultrahigh V_{oc} of 2.05 V, as shown in Fig. 7c.

Besides, some other small molecules, such as the π-conjugated Lewis base 6TIC-4F, which contains a strong electron-donating core and 2 electron-withdrawing units, were dissolved in the anti-solvent to passivate uncoordinated defects on the surface/grain boundaries *via* the direct coordination of N atoms possessing lone pair electrons with the lead ion through the formation of Lewis adducts, thereby suppressing the non-radiative recombination and further increasing the PV performance.[90] Later, Zhang *et al.* fabricated efficient and stable $CsPbI_{1.5}Br_{1.5}$ IPSCs (Fig. 7g) with a PCE of 14.05% and V_{oc} of 1.29 V by incorporating an organic dye, *i.e.*, fluorescein isothiocyanate (FITC), as a passivator in the perovskite precursor (Fig. 7e).[91] The carboxyl and thiocyanate groups of FITC not only minimized the trap states by forming interactions with the uncoordinated Pb^{2+} ions, as illustrated by the mechanism in Fig. 7f, but also significantly increased the grain sizes and improved the crystallinity of the perovskite films during annealing.

4 CsPbIBr₂-based IPSCs

Inorganic $CsPbIBr_2$ perovskite as the light absorber has attracted tremendous attention due to its high-temperature stability at more than 460 °C and low phase transition temperature of about 100 °C. Ma *et al.* first studied $CsPbIBr_2$ IPSCs and adopted a dual source thermal evaporation process to deposit the $CsPbIBr_2$ perovskite light-absorber.[33] The $CsPbIBr_2$ films with an optical bandgap of 2.05 eV displayed a stable PL emission at 2.00 eV. No low-energy PL feature was observed in the $CsPbIBr_2$ perovskite film, suggesting there is no halide segregation in the Cs mixed-halide perovskites, as depicted in Fig. 8a. The $CsPbIBr_2$ IPSCs without the use of an HTL obtained a PCE of 4.7% under reverse scan and 3.7% under forward scan, showing
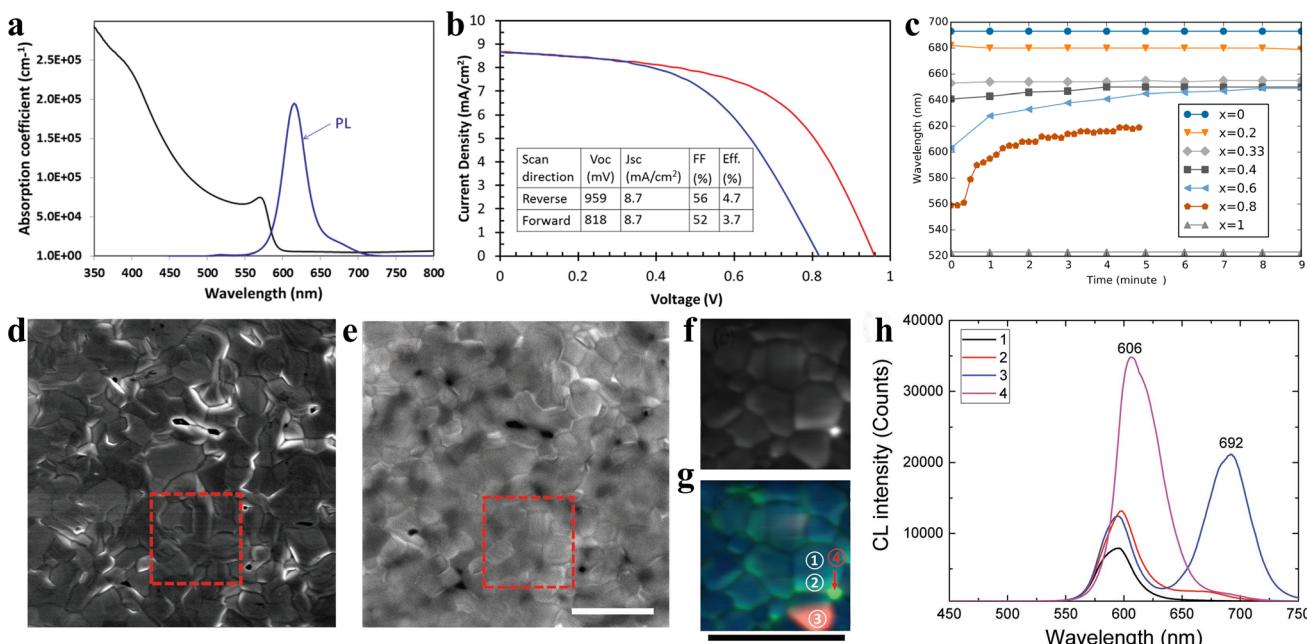

Fig. 8 (a). Absorption coefficient and steady-state PL spectrum of $CsPbIBr_2$ sample. (b). *J–V* curves of the best-performing $CsPbIBr_2$ cell. (a and b) Reproduced with permission.[33] Copyright 2016, Wiley-VCH. (c). PL peak position as a function of time for $CsPb(Br_xI_{1-x})_3$ materials under ~l sun illumination. Reprinted with permission.[44] Copyright 2016, the American Chemical Society. (d) Secondary electron SEM image and (e) CL PMT mapping of the $CsPbIBr_2$ film (1024 × 1024 pixels (≈11 nm on a side); dwell time 50 μs per pixel) with the electron beam acceleration voltage of 5 kV and current of 799 pA. The square region in d was further studied by CL spectrum mapping with different spectral windows of 530–630 nm (pixel size of 40 nm × 40 nm; dwell time of 10 ms). (g). Superposition of (f). (h). CL spectra for the area inside a $CsPbIBr_2$ grain (GI; region ① in (g)), grain boundary (GB; region ② in (g)), and I-rich phase (areas ③ and ④ in (g)). All the scale bars are 3 μm. (d–h) Reproduced with permission.[99] Copyright 2017, Wiley-VCH.

Table 2 Doping/low-temperature fabrication of CsPbIBr$_2$ films and PV performance of the corresponding IPSCs

Device architecture	Deposition method	Active area (cm^2)	PCE (%)	J_{sc} (mA cm^{-2})	V_{oc} (V)	FF (%)	Stability	Year (ref.)
FTO/c-TiO$_2$/CsPbIBr$_2$ (@250 °C)/Au	Dual source evaporation	0.159	4.7	8.7	0.959	56	—	2016 (ref. 33)
FTO/bl-TiO$_2$/mp-TiO$_2$/CsPbIBr$_2$ (@300 °C)/Spiro-OMeTAD/Au	Spray assisted two-step solution	0.159	6.3	7.8	1.127	72	—	2016 (ref. 98)
FTO/In$_2$S$_3$/CsPbIBr$_2$ (@160 °C)/Spiro-OMeTAD/Ag	Spin-coating	0.11	5.59	7.76	1.09	65.94	—	2019 (ref. 100)
FTO/c-TiO$_2$/CsPbIBr$_2$ (@320 °C)/Spiro-OMeTAD/Au	A gas-assisted method	0.16	8.02	9.69	1.227	67.4	—	2017 (ref. 99)
FTO/NiO$_x$/CsPbIBr$_2$ (@160 °C)/MoO$_x$/Au	One-step solution	0.09	5.52	10.56	0.85	62	—	2017 (ref. 101)
FTO/NiO$_x$/CsPbIBr$_2$ (@160 °C)/ZnO/Al	Single-step method	0.04	5.08	8.53	0.97	61.4	—	2018 (ref. 118)
ITO/SnO$_2$/CsPbIBr$_2$ (@100 °C)/Spiro-OMeTAD/Au	Spin-coating (CB anti-solvent)	0.16	9.5	11.52	1.19	69	—	2018 (ref. 119)
FTO/c-TiO$_2$/m-TiO$_2$/CsPbIBr$_2$ (@350 °C)/carbon	Two-step solution	0.09	7.36	13.15	0.99	57	Decreased by 8% of initial PCE value	2018 (ref. 111)
FTO/c-TiO$_2$/m-TiO$_2$/CsPb$_{0.9}$Sn$_{0.1}$IBr$_2$ (@350 °C)/carbon	Two-step sequential solution-phase process	0.09	11.33	14.30	1.26	63	The encapsulated PSCs exhibited almost no degradation after being kept for >3 months at RT	2017 (ref. 110)
ITO/SnO$_2$/C$_{60}$/CsPb$_{0.75}$Sn$_{0.25}$IBr$_2$ (@150 °C)/Spiro-OMeTAD/Au	Spin-coating (CB anti-solvent)	0.10	11.53	12.57	1.21	75.8	Maintained over 90% of the initial PCE after 120 min illumination without encapsulation	2018 (ref. 102)
ITO/SnO$_2$/CsPb$_{0.7}$Sn$_{0.3}$IBr$_2$ (@160 °C)/Spiro-OMeTAD/Au	One-step spin-coating	0.06	14.1	15.5	1.18	76.7	Retained over 75% of original PCE after 10 days exposure to air	2022 (ref. 120)
FTO/c-TiO$_2$/CsPbIBr$_2$ (@100 °C)/carbon	One-step spin-coating	0.09	6.55	9.11	1.142	63	Retained 95% initial efficiency after 288 h of storage	2018 (ref. 103)
ITO/NH$_4$Cl–ZnO/CsPbIBr$_2$ (@160 °C)/Spiro-OMeTAD/Ag	One-step spin-coating	0.11	10.16	11.52	1.27	69.17	Remained almost 70% of the initial value after storage for 800 h in a cabinet (RH: 15%, T: 25 °C)	2020 (ref. 106)
FTO/SnO$_2$/Cs$_{0.99}$MA$_{0.01}$PbIBr$_2$ (@150 °C)/Spiro-OMeTAD/Au	One-step spin-coating	0.06	10.47	11.94	1.21	72.5	Retained 84% of initial PCE after 30 days	2020 (ref. 104)
ITO/c-TiO$_2$/CsPbIBr$_2$ (@160 °C)/carbon	One-step spin-coating (Zn(Ac)$_2$-doped)	0.12	10.65	11.80	1.291	70	Maintained 95% of starting PCE value after 30 days with continuous aging	2022 (ref. 121)
ITO/SnO$_2$/MgO/CsPbIBr$_2$ (@160 °C)/Spiro-OMeTAD/Ag	One-step spin-coating	0.11	11.04	11.70	1.36	69.35	—	2020 (ref. 107)
FTO/c-TiO$_2$/CsPbIBr$_2$ (@160 °C)/Spiro-OMeTAD/Au	One-step spin-coating	0.09	10.78	11.63	1.25	74	—	2020 (ref. 105)
FTO/c-TiO$_2$/Li–CsPbIBr$_2$ (@280 °C)/CuPc/carbon	One-step spin-coating	0.071	9.25	10.27	1.22	74	Maintained 96% of initial PCE after being exposed to air with RH of 40% at 60 °C for one month	2019 (ref. 112)
FTO/c-TiO$_2$/CsPbIBr$_2$ (@160 °C)/carbon	One-step spin-coating	0.09	9.04	10.87	1.26	66	Maintained 95% of initial PCE after 7d storage	2020 (ref. 113)
FTO/c-TiO$_2$/Rb or Ac co-doped CsPbIBr$_2$ (@250 °C)/carbon	One-step spin-coating	0.09	10.78	11.74	1.37	67	Retained 98% of initial PCE after storage for 7 days	2021 (ref. 114)

Table 2 (Contd.)

Device architecture	Deposition method	Active area (cm^2)	PCE (%)	J_{sc} (mA cm^{-2})	V_{oc} (V)	FF (%)	Stability	Year (ref.)
FTO/c-TiO$_2$/CsI(PbBr$_2$)$_{0.95}$(CoCl$_2$)$_{0.05}$ (@250 °C)/Spiro-OMeTAD/Ag	One-step spin-coating	0.07	10.43	12.48	1.25	66.88	Maintained above 90% of initial PCE for 25 days in the air at 25 °C and RH = 20% without encapsulation	2020 (ref. 115)
FTO/c-TiO$_2$/CsPb$_{0.99}$Zn$_{0.01}$IBr$_2$ (@250 °C)/Spiro-OMeTAD/Ag	One-step spin-coating	0.07	10.51	11.92	1.28	69	Maintained 91% of initial PCE after 30 days without encapsulation and stored at 25 °C under ambient conditions with RH of 20%	2021 (ref. 117)
FTO/c-TiO$_2$/CsPbIBr$_2$-0.50% Cu (@225 °C)/Spiro-OMeTAD/Ag	One-step spin-coating	0.0625	10.4	12.8	1.21	67.1	Retained almost 75% of initial PCE when heated at 90 °C in ambient atmosphere with 30% humidity	2020 (ref. 116)
ITO/ZnO/CsPbIBr$_2$ (@140 °C)/Spiro-OMeTAD/Au	One-step spin-coating (vacuum-assisted low-temperature engineering)	0.04	11.01	11.34	1.289	75.31	Retained over 87% of initial PCE after being continuously heated at 80 °C in an inert atmosphere for 80 days without encapsulation	2022 (ref. 122)
FTO/c-TiO$_2$/CsPbIBr$_2$ (@150 °C)/ZnPc/carbon	Two-step spin-coating (CB and IPA mixed anti-solvent)	0.09	8.48	10.33	1.23	66.9	Retained about 90% of initial efficiency after storage at 20% RH in air for 30 days	2022 (ref. 123)

a large hysteresis, as shown in Fig. 8b. Later, the same group deposited CsPbIBr$_2$ films using the spray-assisted-solution method and achieved a PCE of 6.3% with negligible hysteresis.[98] However, it was found that for the CsPb(Br$_x$I$_{1-x}$)$_3$ family, for $x > 0.4$, the phase segregated into I-rich and Br-rich phases under illumination (Fig. 8c).[44] Later, Li *et al.* observed phase segregation into an I-rich phase both at the GBs on the film surface and in the film bulk, in the form of clusters.[99] A high density of mobile ions generated by phase segregation quickly moves along the GBs as ion migration "highways", and finally piles up at the CsPbIBr$_2$/TiO$_2$ interface, resulting in the formation of larger injection barriers, which hamper electron extraction and lead to strong J–V hysteresis in the IPSCs (Fig. 8d–h). This explained why the planar CsPbIBr$_2$ IPSCs exhibited severe hysteresis in the efficiency measurement, showing a PCE of up to 8.02% in the reverse scan and reduced PCE of 4.02% in the forward scan. Combining all these studies, it can be concluded that while phase separation may occur, it seems to depend on the particular films involved and how they are prepared. Table 2 summarizes the doping/low-temperature fabrication of CsPbIBr$_2$ films and the PV performance of the corresponding IPSCs.

4.1 Preparation of CsPbIBr$_2$ films at low temperature

The high-temperature preparation of CsPbIBr$_2$ is a major obstacle for practical applications and flexible devices. Hence, it is urgent to develop processes for the preparation of CsPbIBr$_2$ perovskite layers at low temperature.[100] A new device structure (FTO/NiO$_x$/CsPbIBr$_2$/MoO$_x$/Au) of all-inorganic PSCs was developed by using a low-temperature stable-transition-film (STF) (Fig. 9a) to prepare a highly dense and pinhole-free CsPbIBr$_2$ thin film with high crystalline quality (Fig. 9b).[101] There was no phase separation in this film, but the hysteresis effect still occurred. The PCE of the device rapidly declined in the first 20 s, and gradually reached equilibrium within 100 s, which may be due to light-induced segregation. The low work function MoO$_x$ (4.3 eV) cathode buffer layer with ultra-thin thickness (4 nm) resulted in a decrease in the Schottky barrier, contact resistance and interface trap-state density (Fig. 9c), which increased the PCE of the IPSCs from 1.3% to 5.52%. Later, a series of CsPb$_{1-x}$Sn$_x$IBr$_2$ perovskite alloys was prepared through a one-step anti-solvent method at a lower annealing temperature (150 °C), which presented tunable bandgaps from 2.04 to 1.64 eV.[102] Finally, the optimal CsPb$_{0.75}$Sn$_{0.25}$IBr$_2$ perovskite with $E_g = 1.78$ eV exhibited a homogeneous and densely crystallized morphology.

Perovskite precursor engineering is an effective strategy to reduce the temperature for the fabrication of CsPbIBr$_2$ thin films. For example, pure-phase and full-coverage CsPbIBr$_2$ films could be obtained at a temperature as low as 100 °C by controlling the precursor solution aging time in one-step spin-coating method.[103] The carbon-based IPSCs with these CsPbIBr$_2$ films delivered a PCE of 6.55%. Later, a low-temperature seed-assisted growth (SAG) method was reported for high-quality perovskite films by treating the CsPbIBr$_2$ precursor film with methylammonium halides (MAX, X = I, Br,
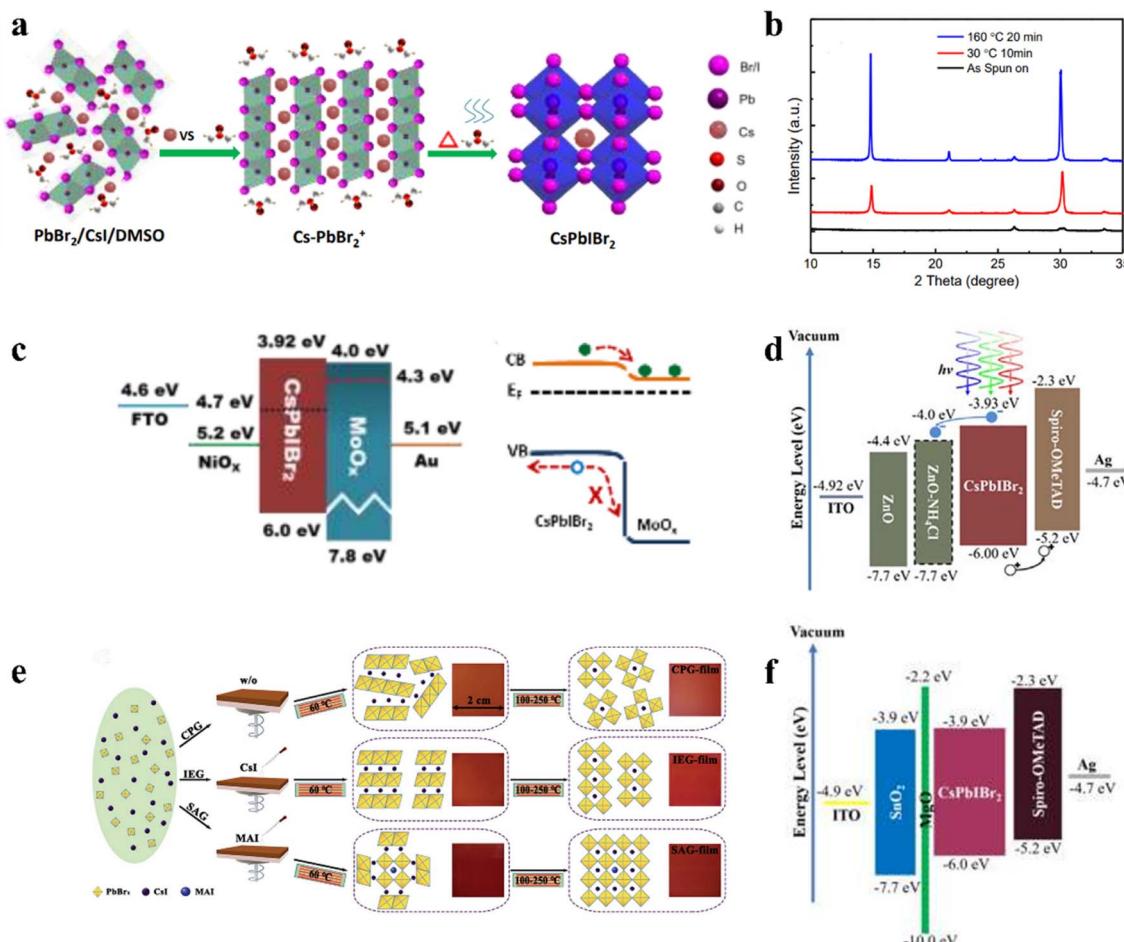
Fig. 9 (a). CsPbIBr$_2$ crystal growth mechanism. (b). XRD patterns of film structural evolution process. (c). Energy band diagram and surface energy bands bend downwards at the CsPbIBr$_2$/MoO$_x$ interface. (a–c) Reproduced with permission.[101] Copyright 2017, Elsevier. (d). Energy level diagrams of the device. Reproduced with permission.[106] Copyright 2020, Wiley-VCH. (e). Schematic illustration of different fabrication methods for CsPbIBr$_2$ films. Reproduced with permission.[104] Copyright 2020, Wiley-VCH. (f). Energy band diagrams of the CsPbIBr$_2$ solar cells with MgO passivation layer. Reproduced with permission.[107] Copyright 2020, Wiley-VCH.

and Cl), followed by annealing treatment, during which MA-perovskite seeds were formed and acted as nuclei for the growth of the CsPbIBr$_2$ perovskite, as shown by the mechanism in Fig. 9e. The MABr-treated CsPbIBr$_2$ perovskite (Pvsk-Br) processed at the low temperature of 150 °C showed an excellent surface morphology with micrometer-sized grains, resulting in long carrier lifetime and low trap density.[104] In addition, the incorporation of n-butylammonium iodide (BAI) as an additive in the CsPbIBr$_2$ precursor not only improved the crystallization and morphology of the perovskite layers to reduce the trap density and restrain the nonradiative recombination, but also decreased the annealing temperature.[105] Consequently, the CsPbIBr$_2$ IPSCs fabricated at 160 °C with an optimal BAI concentration of 0.1% exhibited a PCE of 10.78% and V_{oc} of 1.25 V.

Simultaneous optimization of the perovskite layer and the ETL is an efficient way to reduce the energy losses and improve the V_{oc} for high-performance CsPbIBr$_2$ IPSCs. Introducing a trace of ammonium chloride (NH$_4$Cl) into a sol–gel-derived ZnO as ETL could simultaneously improve the V_{oc}, FF, and

PCE of the CsPbIBr$_2$ IPSCs.[106] The NH$_4$Cl-modified ZnO ETL exhibited a higher electron mobility and reduced work function, leading to a more suitable energy-level alignment between the perovskite and ETL, as shown in Fig. 9d. Finally, the CsPbIBr$_2$ IPSCs with the configuration of ITO/NH$_4$Cl-modified ZnO/CsPbIBr$_2$/Spiro-OMeTAD/Ag under a low fabrication temperature of 160 °C achieved a PCE of 10.16% and outstanding V_{oc} to 1.27 V. Later, the same group reported that the insertion of an ultrathin wide band MgO layer between the SnO$_2$ ETL and CsPbIBr$_2$ photo-absorber not only can passivate the undesirable recombination, and thereby enhance the V_{oc}, but also provide a better substrate for CsPbIBr$_2$ growth to reduce the interface δ-phase perovskite.[107] Furthermore, the tunneling effect and better alignment effectively blocked holes and accelerated the movement of electrons to the electrode, as shown in Fig. 9f.

4.2 Doping strategies for high-quality CsPbIBr$_2$ films

Under the guidance of t, compositional engineering of ABX$_3$ is another way to modulate the crystallization of inorganic
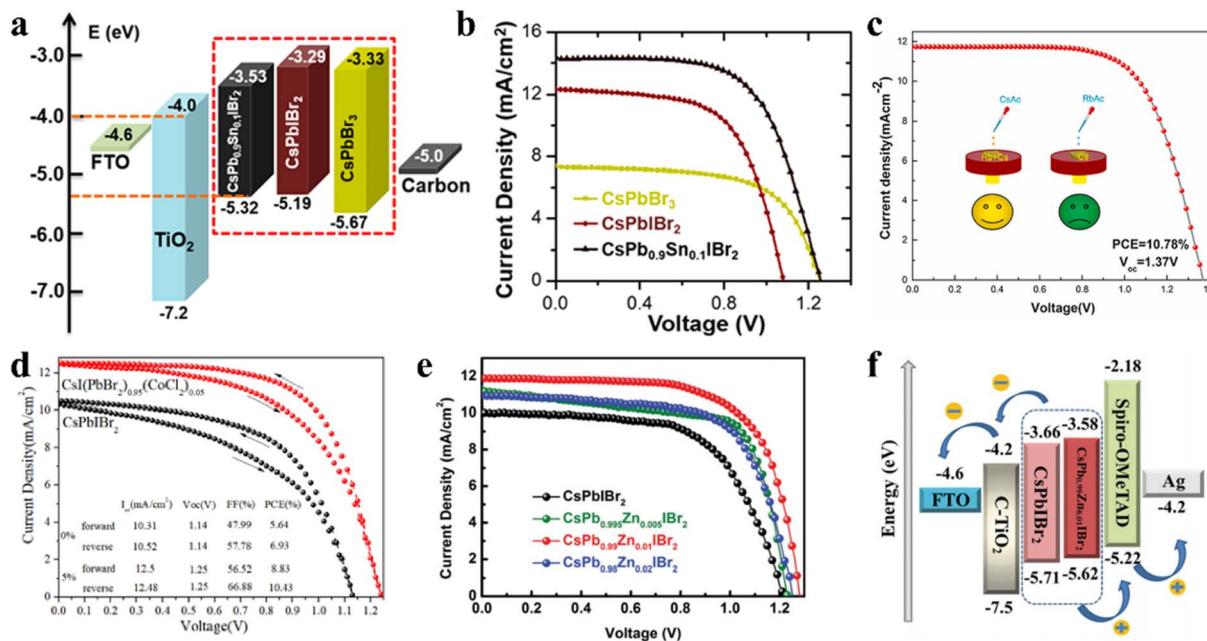
Fig. 10 (a). Energy level diagrams of IPSCs. (b). $J-V$ plots of IPSCs based on CsPbBr$_3$, CsPbIBr$_2$, and CsPb$_{0.9}$Sn$_{0.1}$IBr$_2$, respectively. (a and b) Reprinted with permission.[110] Copyright 2017, the American Chemical Society. (c). $J-V$ curves of IPSCs with multi-source Rb/Ac-doped CsPbIBr$_2$ films. Reproduced with permission.[114] Copyright 2021, Elsevier. (d). $J-V$ curves of optimal CsPbIBr$_2$ and CsI(PbBr$_2$)$_{1-x}$(CoCl$_2$)$_x$ devices under forward and reverse scans. Reproduced with permission.[115] Copyright 2020, Elsevier. (e). $J-V$ curves of the CsPb$_{1-x}$Zn$_x$IBr$_2$ ($x = 0$, 0.005, 0.01 and 0.02) IPSCs under simulated AM1.5G illumination. (f). Corresponding energy level diagrams with CsPbIBr$_2$ and CsPb$_{0.99}$Zn$_{0.01}$IBr$_2$ devices. (e and f) Reproduced with permission.[117] Copyright 2021, The Royal Society of Chemistry.

perovskite films.[108,109] The introduction of different dopants can modify the surface of the perovskite crystal or incorporate them into the crystal lattice to replace one of the substituents. Doping CsPbIBr$_2$ with Mn^{2+} or Sn^{2+} can narrow the bandgap and extend the light response region. A novel CsPb$_{0.9}$Sn$_{0.1}$IBr$_2$ perovskite with an E_g of 1.79 eV (Fig. 10a) was prepared through a convenient two-step sequential solution-phase process in ambient air without the need for a glovebox or humidity control.[110] Consequently, the CsPb$_{0.9}$Sn$_{0.1}$IBr$_2$ IPSCs exhibited a PCE of 11.33% and V_{oc} of 1.26 V, with a voltage loss of only 0.53 V (Fig. 10b), which is very low for a Br-rich perovskite material. The high V_{oc} is mainly due to the better energy level matching between the VBM of the perovskite and the CBM of the ETL. Later, an Mn-doped CsPb$_{1-x}$Mn$_x$I$_{1+2x}$Br$_{2-2x}$ perovskite was synthesized in the ambient atmosphere without any humidity control.[111] The Mn-doped films with appropriate dopant concentration showed better crystallinity and morphology, and a slightly decreased E_g (1.85 eV instead of 1.89 eV without Mn).

In addition, the Li doping strategy can improve the optical, morphological and electronic properties of CsPbIBr$_2$ films.[112] The Li-doped CsPbIBr$_2$ films possess low trap-state densities and long carrier lifetime, contributing to a lower energy loss and a higher charge collection efficiency. In another study, by employing Zn substitution, carbon-based and HTL-free CsPbIBr$_2$ IPSCs exhibited a PCE of 9.04% and 8.09% under low temperature annealing conditions (160 °C and 100 °C, respectively), as reported by Jiang et al.[113] Later, they reported simultaneous cation/anion doping in a CsPbIBr$_2$ film (Fig. 10c). The Rb/Ac co-doped CsPBIBr$_2$ IPSCs exhibited a PCE of 10.78%

with a large V_{oc} of 1.37 V, originating from the long carrier lifetime and low recombination.[114] To slow down the rapid formation and growth of CsPbIBr$_2$ crystals, CoCl$_2$ was used as a morphology controller.[115] The slow crystallization resulted in low trap states and grain boundary in the CsPbIBr$_2$ films, reducing the E_{loss} and enhancing the V_{oc} by up to 1.25 V (Fig. 10d).

By doping an appropriate amount of Cu^{2+} (0.50 at%) in the CsPbIBr$_2$ perovskite lattice, the high-quality CsPbIBr$_2$ film showed increased crystallinity with expanded grain sizes, optimized energy level alignment, decreased trap density, and reduced charge recombination.[116] Consequently, the CsPbIBr$_2$-0.50% Cu-based device with the architecture of FTO/c-TiO$_2$/CsPbIBr$_2$-0.50% Cu/Spiro-OMeTAD/Ag exhibited a PCE of 10.4% and retained 75% of its initial PCE when heated at 90 °C in an ambient atmosphere with 30% humidity. In addition, Long et al. incorporated ZnBr$_2$ in the CsPbIBr$_2$ perovskite precursor and obtained CsPb$_{1-x}$Zn$_x$IBr$_2$ perovskite films using a one-step spin-coating method.[117] Zn^{2+} doping not only can modulate the crystallization of the CsPbIBr$_2$ perovskite film and improve the morphology to suppress charge recombination and decrease the trap states, but also regulate the energy band level of CsPbIBr$_2$, which improved the built-in potential and V_{oc} of the CsPbIBr$_2$ IPSCs (Fig. 10e and f).

4.3 Strategies for improving the performance of CsPbIBr$_2$-IPSCs

Interfacial recombination and nonradiative recombination in CsPbIBr$_2$ IPSCs hinder the device performance. Accordingly, an
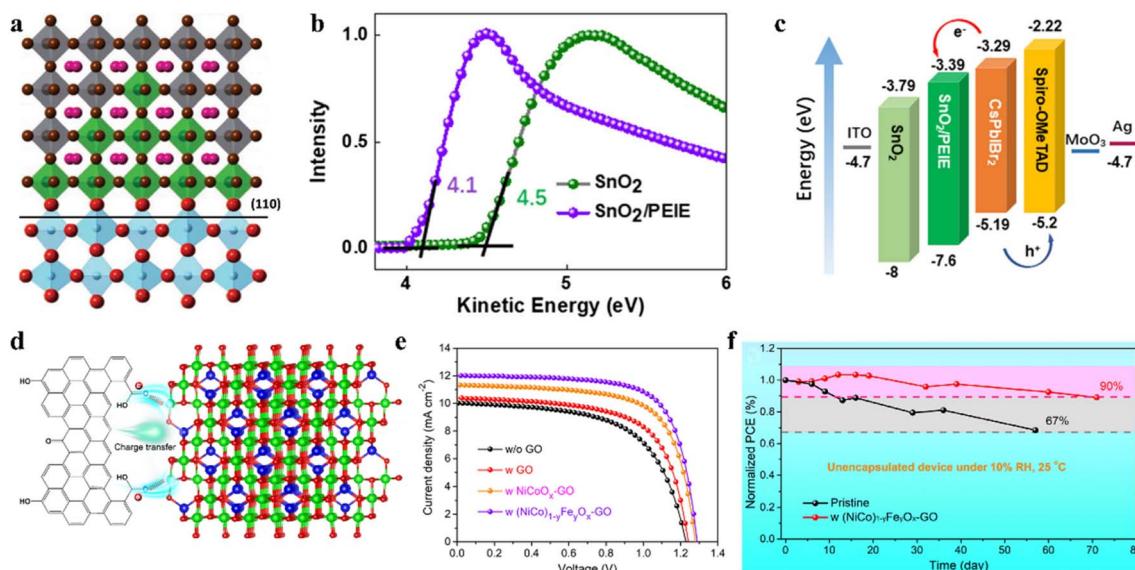
Fig. 11 (a). Schematic diagram depicting the SIM on the (110) crystal plane of rutile-TiO_2 (for octahedra, grey: PbI_2Br_4, green: $SmBr_6$, blue: TiO_6; for spheres, and pink: Cs). Reproduced with permission.[129] Copyright 2018, Wiley-VCH. b. UPS spectra of SnO_2 and SnO_2/PEIE. (c). Energy-level diagram of IPSCs. (b and c) Reproduced with permission.[132] Copyright 2021, Wiley-VCH. (d). Schematic diagram of charge transfer from GO to inorganic NPs. (e). Characteristic $J-V$ curves of various solar cells. (f). Long-term stability of IPSCs. (d–f) Reproduced with permission.[134] Copyright 2021, Wiley-VCH.

effective way to suppress the interfacial recombination is to construct more suitable energy level alignments between the perovskite film and the ETL or HTL.[124-128] For example, a surface modification strategy was proposed for the ETL/perovskite interface by employing $SmBr_3$, wherein a gradient energy band is formed at the interface with an outstanding hole-blocking effect, as shown by the mechanism in Fig. 11a.[129] $SmBr_3$ interface modification could not only improve the charge extraction, but also suppressed the charge recombination occurring at the interface and the nonradiative recombination inside the perovskite material. In another study, band alignment engineering at the TiO_2/$CsPbIBr_2$ heterojunction by modifying TiO_2 with CsBr clusters was reported.[130] The CsBr modifier causes a beneficial increase in the CBM from -4.00 to -3.81 eV for the TiO_2 ETL, thus promoting favorable band alignment at the heterojunction, suppressing recombination, and improving the extraction and transport of charge carriers. Table 3 summarizes several strategies for the preparation of high-quality $CsPbIBr_2$ films and the PV performance of the corresponding IPSCs.

An interface engineering process was developed for SnO_2 ETL surface passivation by employing an $SnCl_2$ solution.[131] Surface passivation of SnO_2 can not only accelerate electron extraction from the perovskite film, but also effectively suppress the recombination at the interface between the $CsPbIBr_2$ perovskite and SnO_2 due to the higher recombination resistance. Later, an interfacial engineering strategy through the insertion of a thin polyethylenimine ethoxylated (PEIE) film between the SnO_2 ETL and perovskite film was employed to reduce the energy loss in $CsPbIBr_2$ IPSCs.[132] The PEIE as a modifier showed positive effects on the device performance

owing to several reasons, as follows: (1) the interactions between the amino groups of PEIE and $CsPbIBr_2$ film can improve the crystallinity and enlarge the grain sizes of the perovskite during film formation. (2) The favorable energy-level alignment between SnO_2/PEIE and $CsPbIBr_2$ perovskite can maximize the device built-in potential (Fig. 11b). (3) The passivation effects of PEIE on the perovskite can alleviate the nonradiative recombination at the interface and enhance the charge extraction ability (Fig. 11c). Finally, the SnO_2/PEIE-based $CsPbIBr_2$ IPSCs showed a remarkable V_{oc} of 1.29 V and PCE of 11.2%. Moreover, the SnO_2/PEIE-based $CsPbIBr_2$ IPSCs maintained over 80% of their initial value after continuous one sun illumination for 500 h. Besides, a CsBr dual-interface modification strategy was used to modify both surfaces of the $CsPbIBr_2$ perovskite with the traditional configuration of FTO/TiO_2/$CsPbIBr_2$/Spiro-OMeTAD/Au.[133] The TiO_2/perovskite interface modification reduced the pinhole and trap-state densities, and regulation of perovskite/Spiro-OMeTAD produced a smoother surface and better crystallinity. Consequently, the synergistic effects of both modifications led to a PCE of 10.33% with a promising V_{oc} of 1.24 V. In addition, the optimized $CsPbIBr_2$ IPSCs retained 60% of their initial efficiency after 60 h of aging in the ambient atmosphere.

In addition to optimizing the ETL/perovskite interface, perovskite/carbon interfacial engineering can boost the performance of $CsPbIBr_2$ IPSCs. For instance, inorganic $(NiCo)_{1-y}$-Fe_yO_x nanoparticle-decorated graphene oxide (GO) was used as a hole collection layer in all-inorganic $CsPbIBr_2$ PSCs with the architecture of FTO/c-TiO_2/$CsPbIBr_2$/NP-GO/carbon.[134] The introduction of high-valance-state Fe^{3+} in $NiCoO_x$ induced the formation of more interstitial oxygen atoms and withdrew some

Table 3 Strategies for the preparation of high-quality $CsPbIBr_2$ films and the PV performance of the corresponding IPSCs

Device architecture	Deposition method	Active area (cm^2)	PCE (%)	J_{sc} (mA cm^{-2})	V_{oc} (V)	FF (%)	Stability	Year (ref.)
FTO/c-TiO$_2$/CsPbIBr$_2$ (@280 °C)/carbon	Spin-coating (CsI treatment)	0.09	9.16	10.66	1.245	69	Retained 90% over 60 days and 97% over 7 days of initial efficiency, stored controllably in ≈45% RH at 25 °C or 85 °C at zero humidity, respectively	2018 (ref. 141)
FTO/NiO$_x$/CsPbIBr$_2$ (@160 °C)/ZnO/Al	Single-step method	0.04	5.08	8.53	0.97	61.4	—	2018 (ref. 118)
FTO/c-TiO$_2$/CsPbIBr$_2$ (@280 °C)/carbon	One-step spin-coating (light-process)	0.09	8.60	11.17	1.283	60	—	2019 (ref. 142)
FTO/c-TiO$_2$/CsPbIBr$_2$ (@120 °C)/Spiro-OMeTAD/Au	Spin-coating (DEE anti-solvent)	0.10	9.17	10.24	1.20	74.6	Maintained 90% of the initial PCE in 40% humidity ambient	2019 (ref. 143)
ITO/SnO$_2$/CsPbIBr$_2$ (@280 °C)/Spiro-OMeTAD/Ag	One-step spin-coating (pre-heating process)	—	9.86	10.69	1.267	71	Retained ~80% of initial efficiency over 72 h	2019 (ref. 144)
FTO/c-TiO$_2$(SmBr$_3$)/CsPbIBr$_2$ (@225 °C)/Spiro-OMeTAD/Au	One-step spin-coating	0.09	10.88	12.75	1.17	73	—	2019 (ref. 129)
FTO/c-TiO$_2$(CsBr)/CsPbIBr$_2$ (@280 °C)/carbon	Two-step spin-coating	0.09	10.71	11.80	1.261	72	—	2019 (ref. 130)
ITO/SnO$_2$/CsPbIBr$_2$ (@160 °C)/carbon	One-step spin-coating	0.08	7.00	8.50	1.23	67	Retained 95.5% of initial performance at 90 °C in air without encapsulation	2019 (ref. 131)
FTO/c-TiO$_2$/CsPbIBr$_2$ (@160 °C)/Spiro-OMeTAD/Au	One-step spin-coating	0.09	7.31	8.80	1.28	64.9	—	2018 (ref. 137)
FTO/c-TiO$_2$/CsPbIBr$_2$ (@260 °C)/NP-GO/carbon	One-step spin-coating	0.09	10.95	12.03	1.29	70.58	Retained 90% of initial PCE after aging in 10% RH air condition for 70 days without encapsulation	2021 (ref. 134)
ITO/c-TiO$_2$/CsPbIBr$_2$ (@160 °C)/BHJ/carbon	One-step spin-coating	—	11.54	11.79	1.31	74.47	—	2021 (ref. 135)
FTO/c-TiO$_2$/CsPbIBr$_2$ (@280 °C)/CsPbI$_3$ QDs/Spiro-OMeTAD/Au	One-step spin-coating	—	10.32	11.09	1.20	77.7	Maintained 90% of initial PCE without encapsulation devices stored in air (RH: 25%, T: 25 °C)	2021 (ref. 136)
FTO/c-TiO$_2$/PEG:CsPbIBr$_2$ (@200 °C)/Spiro-OMeTAD/Ag	One-step spin-coating	0.078	11.10	12.25	1.21	74.82	Retained over 90% of the initial PCE after 600 h storage in ambient condition without encapsulation	2020 (ref. 138)
FTO/c-TiO$_2$/CsPbIBr$_2$ (@280 °C)/Spiro-OMeTAD/Au	One-step spin-coating	0.16	10.1	12.11	1.13	74	Retained 96% of initial PCE for 30 days under 40% RH	2021 (ref. 139)
FTO/c-TiO$_2$/CsPb(SO$_3$)IBr$_2$ (@225 °C)/Spiro-OMeTAD/Au	One-step spin-coating	0.09	10.57	12.27	1.21	71	Maintained over 80% of initial PCE after aging for 198 h in air without encapsulation	2020 (ref. 140)
FTO/c-TiO$_2$/CsPbIBr$_2$ (@225 °C)/Spiro-OMeTAD/Au	One-step spin-coating	0.09	10.04	11.35	1.23	72	—	2021 (ref. 145)
FTO/c-TiO$_2$/CsPbIBr$_2$ (@260 °C)/carbon	One-step spin-coating	0.09	10.61	11.58	1.293	70.86	Remained 56% of the initial PCE over 28 h with a humidity of 50% and a temperature of 25 °C	2022 (ref. 146)

Table 3 (Contd.)

Device architecture	Deposition method	Active area (cm^2)	PCE (%)	J_{sc} (mA cm^{-2})	V_{oc} (V)	FF (%)	Stability	Year (ref.)
FTO/c-TiO$_2$/CsPbIBr$_2$ (@260 °C)/carbon	One-step spin-coating (SBTCl post-treatment)	0.09	10.56	11.43	1.327	69.7	After storage in 5% RH without encapsulation over 110 days and persistent light irradiation over 16 h in 50% RH condition	2022 (ref. 147)
FTO/c-TiO$_2$/CsPbIBr$_2$ (@280 °C)/Spiro-OMeTAD/Au	One-step spin-coating (GuaSCN additive)	0.04	10.90	12.05	1.23	73.71	Retained ~95% of initial value after being stored for over 600 h without encapsulation in air	2022 (ref. 148)

electrons from the Ni^{2+}/Co^{2+} ions. The particle electrons for the oxygen-containing groups in the GO surface spontaneously transferred to the inorganic NPs owing to their electropositivity to minimize the charge localization of GO, thus forming p-type-doped GO and an oriented dipole moment from GO to $(NiCo)_{1-y}Fe_yO_x$, as shown by the mechanism in Fig. 11d. Consequently, the NP-GO-tailored CsPbIBr$_2$ IPSCs delivered a PCE of 10.95% and retained 90% of their initial efficiency after aging in 10% RH ambient conditions for 70 days owing to the self-encapsulation effect (Fig. 11e and f). In another study, a thin bulk-heterojunction (BHJ) layer (19 nm) consisting of poly(3-hexylthiophene-2,5-diyl) and [6,6]-phenyl methyl C$_{61}$ butyric acid methyl ester (P3HT:PCBM) was integrated in CsPbIBr$_2$ IPSCs with the configuration of ITO/TiO$_2$/CsPbIBr$_2$/BHJ/carbon.[135] The introduction of the thin BHJ layer led to an expanded light absorption range, better charge transfer dynamics, suppressed interfacial energy loss in the CsPbIBr$_2$/BHJ film and CsPbIBr$_2$/BHJ/carbon, and improved long-term stability. The CsPbIBr$_2$ IPSCs with an integrated BHJ layer showed a PCE of 11.54%.

QDs films can also be adopted as functional layers for PV devices with other bulk absorbers layers. For example, Sr-doped CsPbI$_3$ QDs (Sr-CsPbI$_3$ QDs) were introduced as an interfacial layer in CsPbIBr$_2$ IPSCs to improve the device performance.[136] The Sr-CsPbI$_3$ QDs were synthesized by using $SrCl_2$ as a co-precursor. The modification of the Sr-CsPbI$_3$ QD interface not only optimized the charge transfer process and suppressed the interface recombination between the perovskite and HTL, but also restrained the nonradiative recombination in the CsPbIBr$_2$ perovskite film.

The defect states at the grain boundaries and on the surface of the CsPbIBr$_2$ polycrystalline film led to nonradiative carrier recombination, which reduced the V_{oc} and final PCE of the corresponding PSCs. The combination of functional compounds in the perovskite precursor solution is considered to be an effective method to assist the formation of high-quality perovskite films. The intramolecular interactions between the perovskite precursors and these new compounds have important effects on the crystal dynamics of the perovskite. For example, high-quality CsPbIBr$_2$ films were obtained by mixing a small amount of polyethylene glycol (PEG).[137] PEG can not only improve coverage of the CsPbIBr$_2$ perovskite film on the TiO$_2$ layer, but also improve the wettability of the precursor solution. The self-assembled PEG network can slow down crystal growth and restrain the aggregation of the perovskite crystals during the process of perovskite phase formation, which effectively passivates the defect states at the grain boundaries and surface of the CsPbIBr$_2$ bulk film. Later, the Lewis base PEG was also adopted as an additive to modify a CsPbIBr$_2$ perovskite film. The PEG:CsPbIBr$_2$ film exhibited suppressed non-radiative electron–hole recombination, a favorable energy band structure and less sensitivity to moisture, which originated from the reduced crystallization rate and strong interaction with Pb^{2+} (Fig. 12a). Ultimately, the device based on PEG:CsPbIBr$_2$ delivered a PCE of 11.10%. Moreover, the PEG-modified device showed excellent long-term stability, retaining over 90% of its initial PCE after 600 h storage in
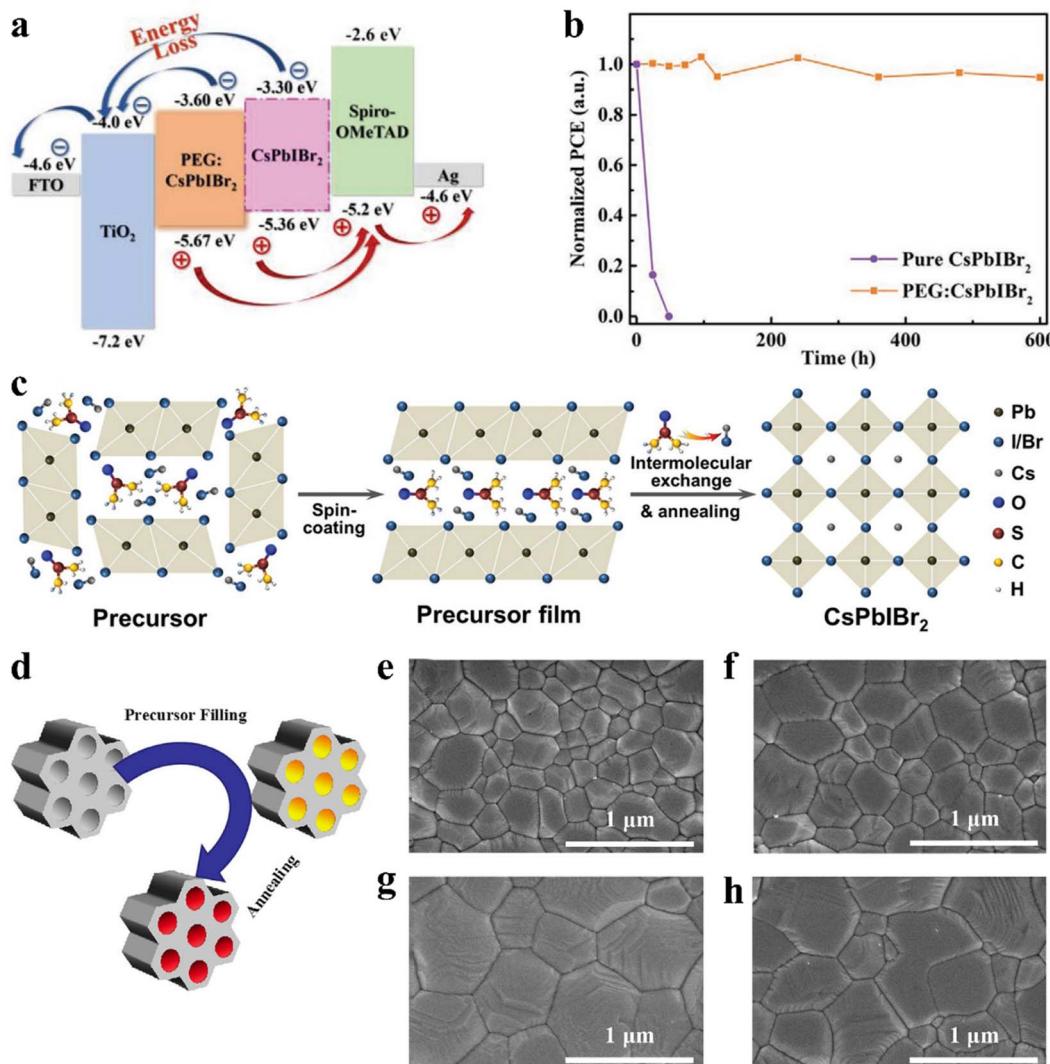
Fig. 12 (a). Corresponding energy band diagrams of the cell. (b). Time-dependent (RH of 35% and temperature of 25 °C) of normalized PCE for the devices with and without PEG. (a and b) Reproduced with permission.[138] Copyright 2020, Wiley-VCH. (c). Illustration of intermolecular exchange strategy. Reproduced with permission.[141] Copyright 2018, Wiley-VCH. (d). Schematic diagram of the nanoconfined crystallization of $CsPbIBr_2$ in ZrSBA-15. Top-view SEM images of various $CsPbIBr_2$ perovskite films: (e). without ZrSBA-15; (f). with 0.01 wt% ZrSBA-15; g. with 0.1 wt% ZrSBA-15; and (h). with 1 wt% ZrSBA-15. (d–h) Reproduced with permission.[145] Copyright 2021, Wiley-VCH.

ambient conditions without encapsulation, as shown in Fig. 12b.[138] In addition, a high-quality $CsPbIBr_2$ perovskite film was prepared by combining both substrate preheat treatment (SPT) and NH_4PF_6 precursor additive engineering.[139] Sulfamic acid sodium salt (SAS) was also utilized as an additive to optimize the $CsPbIBr_2$ perovskite film.[140] SAS not only can regulate the crystallization process, resulting in a high-quality perovskite, but also possibly introduce an additional internal electric field effect, which favors electron transport and injection due to the inhomogeneous ion distribution.

To improve the PV performance of $CsPbIBr_2$ IPSCs, many other effective strategies have been extensively explored, such as post-treatment of the perovskite films, surface passivation and crystallization engineering. An intermolecular exchange strategy for $CsPbIBr_2$ films was presented, wherein an optimized methanol solution of CsI was spin-coated on the

$CsPbIBr_2$ precursor film *via* the conventional one-step solution route (Fig. 12c).[141] The resulting $CsPbIBr_2$ films consisted of high crystallinity with few grain boundaries, which did not exhibit segregation compared to the same films without the CsI treatment exhibiting phase-segregation. A light-processing strategy was developed to produce a full-coverage, pure-phase $CsPbIBr_2$ film.[142] The $CsPbIBr_2$ precursor films formed by the one-step spin-coating route were exposed in a simulated one-sun source for a duration of 60 min, followed by thermal annealing.

In another study, the anti-solvent and organic ion surface passivation strategies were adopted to precisely control the growth of $CsPbIBr_2$ crystals.[143] A high-quality $CsPbIBr_2$ film was successfully obtained by introducing diethyl ether as the anti-solvent to improve the film coverage, crystallization, and homogeneous packing of the grains. Furthermore,

guanidinium surface passivation can restrain the formation of the pinholes by assisting the secondary growth of the CsPbIBr$_2$ film, which can suppress the formation of iodide vacancies and inactivation of the uncoordinated iodide species in the bulk and at the grain boundaries. Guo *et al.* reported a pre-heating-assisted one-step spin-coating method,[144] where during spin-coating, the high-temperature substrate accelerates the volatilization of the solvent molecules, resulting in the complete coverage and higher crystallization of CsPbIBr$_2$ films. By optimizing the substrate-preheating temperature, the IPSCs exhibited a PCE of 9.86% with a stabilized output of 8.78% and high V_{oc} of 1.267 V. Besides, nanoconfined crystallization is considered a novel and effective strategy because of the absence of chemical reactions. 1D ordered mesoporous silica is introduced into inorganic perovskite precursors to facilely induce nanoconfined crystallization, as illustrated by the mechanism in Fig. 12d. Zr-doped SBA-15 (ZrSBA-15) nanoplatelets with suitable sizes were synthesized and added to the perovskite precursors to prepare 1D CsPbIBr$_2$ perovskite monocrystals, facilitating charge transport and extraction.[145] ZrSBA-15 is not only beneficial for the crystallization and morphology of the perovskite (Fig. 12e–h), but also reduces the defect density and improves the film stability.

5 Summary and prospect

Herein, the latest research progress of mixed-halide IPSCs was reviewed, including CsPbI$_x$Br$_y$Cl$_{3-x-y}$- and CsPbIBr$_2$-based IPSCs. Significant progress has been made in the preparation of stable and efficient mixed-halide IPSCs. The bandgaps and stability of mixed-halide perovskites are superior to that of pure halide inorganic perovskites. Compositional engineering has been widely used in mixed-halide IPSCs, which is beneficial to improve the phase stability and reduce the defect density.

Crystallization and interface engineering have been extensively developed to obtain high-quality mixed-halide IPSCs. The combination of functional compounds in the perovskite precursor solution can assist in the formation of high-quality mixed-halide inorganic perovskite films. Intramolecular interactions between the perovskite precursors and these particular compounds have important effects on the crystal dynamics of the perovskite. Moreover, perovskite precursor engineering has been proven to be effective in reducing the temperature for the preparation of mixed-halide inorganic perovskite thin films. In addition, interfacial modification can effectively improve the perovskite phase stability, passivate defects and enhance the performance of mixed-halide IPSCs. Therefore, constructing more suitable energy level alignments between the perovskite film and the ETL or HTL can effectively suppress the interfacial recombination.

The efficiency of the reported mixed-halide IPSCs is significantly lower than that of organic–inorganic hybrid PSCs, and their stabilities are far from reaching commercial PV applications. Thus, effective strategies need to be selected and/or developed to further improve the PCE and stability for facilitating the PV application of mixed-halide IPSCs. At present, the research on large-scale modules is insufficient. For the

manufacturing of large-area PV device modules, the low-temperature preparation of functional layers can simplify the fabrication process and reduce the industrialization cost. For the normal n–i–p structure, TiO$_2$ and SnO$_2$ prepared by low-temperature solution are better choices as the ETLs.

The mixed-halide inorganic perovskites have reasonable bandgaps and show great potential in semitransparent and tandem PV applications. Thus far, there is not enough research on multi-junction tandem and flexible PV applications. To maximize the light spectrum utilization, it is an inevitable choice to develop multi-junction tandem solar cells with mixed-halide inorganic perovskite as the top cells. Because the HTLs, such as undoped HTM and NiO$_x$, can be processed at low temperatures, it is easier to prepare flexible PSCs adopting the inverted p–i–n architecture. Besides, graphene and its derivatives are expected to be utilized as charge transport materials or electrodes in flexible PSCs.

Mixed-halide inorganic perovskites have excellent thermal stability and promising theoretical efficiency. However, their stability lags behind the rapid growth in PCE, and thus becomes the next major challenge. To produce high-quality mixed-halide inorganic perovskite and efficient PV devices, effective strategies should be continuously explored. Once the stability of mixed-halide IPSCs is resolved, either in a single junction or multi-junction tandem with silicon cells, it will be a major development in the PV field.

Conflicts of interest

There are no conflicts to declare.

Acknowledgements

References

1 J. H. Noh, S. H. Im, J. H. Heo, T. N. Mandal and S. Il Seok, *Nano Lett.*, 2013, **13**, 1764–1769.
2 S. D. Stranks, G. E. Eperon, G. Grancini, C. Menelaou, M. J. P. Alcocer, T. Leijtens, L. M. Herz, A. Petrozza and H. J. Snaith, *Science*, 2013, **342**, 341.
3 Q. Lin, A. Armin, R. C. R. Nagiri, P. L. Burn and P. Meredith, *Nat. Photonics*, 2015, **9**, 106.
4 W. Nie, H. Tsai, R. Asadpour, A. J. Neukirch, G. Gupta, J. J. Crochet, M. Chhowalla, S. Tretiak, M. A. Alam and H. Wang, *Science*, 2015, **347**, 522.
5 Q. Dong, Y. Fang, Y. Shao, P. Mulligan, J. Qiu, L. Cao and J. Huang, *Science*, 2015, **347**, 967.
6 D. W. DeQuilettes, S. M. Vorpahl, S. D. Stranks, H. Nagaoka, G. E. Eperon, M. E. Ziffer, H. J. Snaith and D. S. Ginger, *Science*, 2015, **348**, 683.
7 A. K. Jena, A. Kulkarni and T. Miyasaka, *Chem. Rev.*, 2019, **119**, 3036.

8   T. Miyasaka, A. Kojima, K. Teshima and Y. Shirai, *J. Am. Chem. Soc.*, 2009, **131**, 6050.

9   H. Min, M. Kim, S. U. Lee, H. Kim, G. Kim, K. Choi, J. H. Lee and S. Il Seok, *Science*, 2019, **366**, 749.

10 H. Lu, Y. Liu, P. Ahlawat, A. Mishra, W. R. Tress, F. T. Eickemeyer, Y. Yang, F. Fu, Z. Wang, C. E. Avalos, B. I. Carlsen, A. Agarwalla, X. Zhang, X. Li, Y. Zhan, S. M. Zakeeruddin, L. Emsley, U. Rothlisberger, L. Zheng, A. Hagfeldt and M. Grätzel, *Science*, 2020, **370**, eabb8985.

11 H. Min, M. Kim, S.-U. Lee, H. Kim, G. Kim, K. Choi, J. H. Lee and S. Il Seok, *Science*, 2020, **370**, 749.

12 G. Kim, H. Min, K. S. Lee, D. Y. Lee, S. M. Yoon and S. Il Seok, *Science*, 2020, **370**, 108.

13 T. G. P. Jason, J. Yoo1, G. Seo, M. R. Chua, C. S. M. Yongli Lu, F. Rotermund, Y.-Ki Kim, N. JoongJeon, J. S. Correa-Baena, C. B. Juan-Pablo, V. Bulović, S. S. Shin and M. G. Bawendi1, *Nature*, 2021, **590**, 587.

14 J. Jeong, M. Kim, J. Seo, H. Lu, P. Ahlawat, A. Mishra, Y. Yang, M. A. Hope, F. T. Eickemeyer, M. Kim, Y. J. Yoon, I. W. Choi, B. P. Darwich, S. J. Choi, Y. Jo, J. H. Lee, B. Walker, S. M. Zakeeruddin, L. Emsley, U. Rothlisberger, A. Hagfeldt, D. S. Kim, M. Grätzel and J. Y. Kim, *Nature*, 2021, **592**, 381.

15 W. Hui, L. Chao, H. Lu, F. Xia, Q. Wei, Z. Su, T. Niu, L. Tao, B. Du, D. Li, Y. Wang, H. Dong, S. Zuo, B. Li, W. Shi, X. Ran, P. Li, H. Zhang, Z. Wu, C. Ran, L. Song, G. Xing, X. Gao, J. Zhang, Y. Xia, Y. Chen and W. Huang, *Science*, 2021, **371**, 1359.

16 https://www.nrel.gov/pv/assets/pdfs/best-research-cell-efficiencies-rev220630.pdf, n.d., DOI: https://www.nrel.gov/pv/assets/pdfs/best-research-cell-efficiencies-rev220630.pdf.

17 T. Leijtens, G. E. Eperon, S. Pathak, A. Abate, M. M. Lee and H. J. Snaith, *Nat. Commun.*, 2013, **4**, 2885.

18 T. Supasai, N. Rujisamphan, K. Ullrich, A. Chemseddine and T. Dittrich, *Appl. Phys. Lett.*, 2013, **103**, 183906.

19 A. Dualeh, P. Gao, S. Il Seok, M. K. Nazeeruddin and M. Grätzel, *Chem. Mater.*, 2014, **26**, 6160.

20 B. Conings, J. Drijkoningen, N. Gauquelin, A. Babayigit, J. D'Haen, L. D'Olieslaeger, A. Ethirajan, J. Verbeeck, J. Manca, E. Mosconi, F. De Angelis and H. G. Boyen, *Adv. Energy Mater.*, 2015, **5**, 1500477.

21 N. Aristidou, I. Sanchez-Molina, T. Chotchuangchutchaval, M. Brown, L. Martinez, T. Rath and S. A. Haque, *Angew. Chem., Int. Ed.*, 2015, **54**, 8208.

22 E. Smecca, Y. Numata, I. Deretzis, G. Pellegrino, S. Boninelli, T. Miyasaka, A. La Magna and A. Alberti, *Phys. Chem. Chem. Phys.*, 2016, **18**, 13413.

23 N. Aristidou, C. Eames, I. Sanchez-Molina, X. Bu, J. Kosco, M. Saiful Islam and S. A. Haque, *Nat. Commun.*, 2017, **8**, 15218.

24 Y. Rong, L. Liu, A. Mei, X. Li and H. Han, *Adv. Energy Mater.*, 2015, **5**, 1501066.

25 T. A. Berhe, W. N. Su, C. H. Chen, C. J. Pan, J. H. Cheng, H. M. Chen, M. C. Tsai, L. Y. Chen, A. A. Dubale and B. J. Hwang, *Energy Environ. Sci.*, 2016, **9**, 323.

26 N. H. Tiep, Z. Ku and H. J. Fan, *Adv. Energy Mater.*, 2016, **6**, 1501420.

27 P. Yu, W. Zhang, F. Ren, J. Wang, H. Wang, R. Chen, S. Zhang, Y. Zhang, Z. Liu and W. Chen, *J. Mater. Chem. C*, 2022, **10**, 4999.

28 Y. Pan, Y. Zhang, W. Kang, N. Deng, Z. Yan, W. Sun, X. Kang and J. Ni, *Mater. Adv.*, 2022, **3**, 4053.

29 Y. Yuan, G. Yan, R. Hong, Z. Liang and T. Kirchartz, *Adv. Mater.*, 2022, 2108132.

30 J. Ma, M. Qin, P. Li, L. Han, Y. Zhang and Y. Song, *Energy Environ. Sci.*, 2022, **15**, 413.

31 M. Kulbak, D. Cahen and G. Hodes, *J. Phys. Chem. Lett.*, 2015, **6**, 2452.

32 M. Kulbak, S. Gupta, N. Kedem, I. Levine, T. Bendikov, G. Hodes and D. Cahen, *J. Phys. Chem. Lett.*, 2016, **7**, 167.

33 Q. Ma, S. Huang, X. Wen, M. A. Green and A. W. Y. Ho-Baillie, *Adv. Energy Mater.*, 2016, **6**, 1502202.

34 R. J. Sutton, G. E. Eperon, L. Miranda, E. S. Parrott, B. A. Kamino, J. B. Patel, M. T. Hörantner, M. B. Johnston, A. A. Haghighirad, D. T. Moore and H. J. Snaith, *Adv. Energy Mater.*, 2016, **6**, 1502458.

35 Z. Guo, A. K. Jena, G. M. Kim and T. Miyasaka, *Energy Environ. Sci.*, 2022, **15**, 3171.

36 Z. Guo, S. Zhao, N. Shibayama, A. Kumar Jena, I. Takei and T. Miyasaka, *Adv. Funct. Mater.*, 2022, **32**, 2207554.

37 Q. A. Akkerman, V. D'Innocenzo, S. Accornero, A. Scarpellini, A. Petrozza, M. Prato and L. Manna, *J. Am. Chem. Soc.*, 2015, **137**, 10276.

38 G. E. Eperon, R. J. Sutton, A. A. Haghighirad, H. J. Snaith, G. M. Paternò, A. Zampetti and F. Cacialli, *J. Mater. Chem. A*, 2015, **3**, 19688.

39 P. Luo, W. Xia, S. Zhou, L. Sun, J. Cheng, C. Xu and Y. Lu, *J. Phys. Chem. Lett.*, 2016, **7**, 3603.

40 Y. Hu, F. Bai, X. Liu, Q. Ji, X. Miao, T. Qiu and S. Zhang, *ACS Energy Lett.*, 2017, **2**, 2219.

41 H. Li, G. Tong, T. Chen, H. Zhu, G. Li, Y. Chang, L. Wang and Y. Jiang, *J. Mater. Chem. A*, 2018, **6**, 14255.

42 X. Liu, X. Tan, Z. Liu, H. Ye, B. Sun, T. Shi, Z. Tang and G. Liao, *Nano Energy*, 2019, **56**, 184.

43 W. S. Subhani, K. Wang, M. Du and S. F. Liu, *Nano Energy*, 2019, **61**, 165.

44 R. E. Beal, D. J. Slotcavage, T. Leijtens, A. R. Bowring, R. A. Belisle, W. H. Nguyen, G. F. Burkhard, E. T. Hoke and M. D. McGehee, *J. Phys. Chem. Lett.*, 2016, **7**, 746.

45 S. Mariotti, O. S. Hutter, L. J. Phillips, P. J. Yates, B. Kundu and K. Durose, *ACS Appl. Mater. Interfaces*, 2018, **10**, 3750.

46 J. K. Sun, S. Huang, X. Z. Liu, Q. Xu, Q. H. Zhang, W. J. Jiang, D. J. Xue, J. C. Xu, J. Y. Ma, J. Ding, Q. Q. Ge, L. Gu, X. H. Fang, H. Z. Zhong, J. S. Hu and L. J. Wan, *J. Am. Chem. Soc.*, 2018, **140**, 11705.

47 P. K. Nielsen, C. Hemmingsen, S. U. Friis, J. Ladefoged and K. Olgaard, *Peritoneal Dial. Int.*, 1995, **15**, 18.

48 Z. Cheng and J. Lin, *CrystEngComm*, 2010, **12**, 2646.

49 C. Li, X. Lu, W. Ding, L. Feng, Y. Gao and Z. Guo, *Acta Crystallogr., Sect. B: Struct. Sci.*, 2008, **64**, 702.

50 W. Travis, E. N. K. Glover, H. Bronstein, D. O. Scanlon and R. G. Palgrave, *Chem. Sci.*, 2016, **7**, 4548.

51 D. B. Straus, S. Guo, A. M. Abeykoon and R. J. Cava, *Adv. Mater.*, 2020, **32**, 2001069.

52 V. K. Ravi, G. B. Markad and A. Nag, *ACS Energy Lett.*, 2016, **1**, 665.

53 J. Brgoch, A. J. Lehner, M. Chabinyc and R. Seshadri, *J. Phys. Chem. C*, 2014, **118**, 27721.

54 C. C. Stoumpos, C. D. Malliakas, J. A. Peters, Z. Liu, M. Sebastian, J. Im, T. C. Chasapis, A. C. Wibowo, D. Y. Chung, A. J. Freeman, B. W. Wessels and M. G. Kanatzidis, *Cryst. Growth Des.*, 2013, **13**, 2722.

55 A. Filippetti and A. Mattoni, *Phys. Rev. B: Condens. Matter Mater. Phys.*, 2014, **89**, 125203.

56 L. Protesescu, S. Yakunin, M. I. Bodnarchuk, F. Krieg, R. Caputo, C. H. Hendon, R. X. Yang, A. Walsh and M. V. Kovalenko, *Nano Lett.*, 2015, **15**, 3692.

57 K. Heidrich, W. Schäfer, M. Schreiber, J. Söchtig, G. Trendel, J. Treusch, T. Grandke and H. J. Stolz, *Phys. Rev. B*, 1981, **24**, 5642.

58 X. Li, Y. Wu, S. Zhang, B. Cai, Y. Gu, J. Song and H. Zeng, *Adv. Funct. Mater.*, 2016, **26**, 2435.

59 X. Li, F. Cao, D. Yu, J. Chen, Z. Sun, Y. Shen, Y. Zhu, L. Wang, Y. Wei, Y. Wu and H. Zeng, *Small*, 2017, **13**, 1603996.

60 Y. Wang and H. Sun, *Small Methods*, 2017, 1700252.

61 S. Sanchez, N. Christoph, B. Grobety, N. Phung, U. Steiner, M. Saliba and A. Abate, *Adv. Energy Mater.*, 2018, **8**, 1802060.

62 E. M. Hutter, R. J. Sutton, S. Chandrashekar, M. Abdi-Jalebi, S. D. Stranks, H. J. Snaith and T. J. Savenije, *ACS Energy Lett.*, 2017, **2**, 1901.

63 S. Dastidar, S. Li, S. Y. Smolin, J. B. Baxter and A. T. Fafarman, *ACS Energy Lett.*, 2017, **2**, 2239.

64 J. K. Nam, S. U. Chai, W. Cha, Y. J. Choi, W. Kim, M. S. Jung, J. Kwon, D. Kim and J. H. Park, *Nano Lett.*, 2017, **17**, 2028.

65 Y. Li, C. Zhang, X. Zhang, D. Huang, Q. Shen, Y. Cheng and W. Huang, *Appl. Phys. Lett.*, 2017, **111**, 162106.

66 Y. Huang, W. J. Yin and Y. He, *J. Phys. Chem. C*, 2018, **122**, 1345.

67 R. J. Sutton, M. R. Filip, A. A. Haghighirad, N. Sakai, B. Wenger, F. Giustino and H. J. Snaith, *ACS Energy Lett.*, 2018, **3**, 1787.

68 L. Fu, Y. Zhang, B. Chang, B. Li, S. Zhou, L. Zhang and L. Yin, *J. Mater. Chem. A*, 2018, **6**, 13263.

69 H. Zhao, Y. Han, Z. Xu, C. Duan, S. Yang, S. Yuan, Z. Yang, Z. Liu and S. Liu, *Adv. Energy Mater.*, 2019, **9**, 1902279.

70 Y.-T. Yu, S.-H. Yang, L.-H. Chou, I. Osaka, X.-F. Wang and C.-L. Liu, *ACS Appl. Energy Mater.*, 2021, **4**, 5466.

71 S. Dastidar, D. A. Egger, L. Z. Tan, S. B. Cromer, A. D. Dillon, S. Liu, L. Kronik, A. M. Rappe and A. T. Fafarman, *Nano Lett.*, 2016, **16**, 3563.

72 K. Wang, Z. Jin, L. Liang, H. Bian, H. Wang, J. Feng, Q. Wang and S. Frank Liu, *Nano Energy*, 2019, **58**, 175.

73 Y. Wang, X. Liu, T. Zhang, X. Wang, M. Kan, J. Shi and Y. Zhao, *Angew. Chem., Int. Ed.*, 2019, **58**, 16691.

74 Q. Ye, Y. Zhao, S. Mu, F. Ma, F. Gao, Z. Chu, Z. Yin, P. Gao, X. Zhang and J. You, *Adv. Mater.*, 2019, **31**, 1905143.

75 J. Lin, M. Lai, L. Dou, C. S. Kley, H. Chen, F. Peng, J. Sun, D. Lu, S. A. Hawks, C. Xie, F. Cui, A. P. Alivisatos, D. T. Limmer and P. Yang, *Nat. Mater.*, 2018, **17**, 261.

76 H. Wang, H. Bian, Z. Jin, H. Zhang, L. Liang, J. Wen, Q. Wang, L. Ding and S. F. Liu, *Chem. Mater.*, 2019, **31**, 6231.

77 S. Lee, J. Moon, J. Ryu, B. Parida, S. Yoon, D. G. Lee, J. S. Cho, S. Hayase and D. W. Kang, *Nano Energy*, 2020, **77**, 105309.

78 Z. Yao, Z. Xu, W. Zhao, J. Zhang, H. Bian, Y. Fang, Y. Yang and S. Liu, *Adv. Energy Mater.*, 2021, **11**, 2100403.

79 X. Wu, J. Ma, M. Qin, X. Guo, Y. Li, Z. Qin, J. Xu and X. Lu, *Adv. Funct. Mater.*, 2021, **31**, 2101287.

80 X. Wu, F. Qi, F. Li, X. Deng, Z. Li, S. Wu, T. Liu, Y. Liu, J. Zhang and Z. Zhu, *Energy Environ. Mater.*, 2021, **4**, 95.

81 K. Wang, S. Ma, X. Xue, T. Li, S. Sha, X. Ren, J. Zhang, H. Lu, J. Ma, S. Guo, Y. Liu, J. Feng, A. Najar and S. Liu, *Adv. Sci.*, 2022, **9**, 2105103.

82 F. Wang, Z. Qiu, Y. Chen, Y. Zhang, Z. Huang, N. Li, X. Niu, H. Zai, Z. Guo, H. Liu and H. Zhou, *Adv. Mater.*, 2022, **34**, 2108357.

83 J. Ma, M. Qin, Y. Li, X. Wu, Z. Qin, Y. Wu, G. Fang and X. Lu, *Matter*, 2021, **4**, 313.

84 K. Wang, C. Gao, Z. Xu, Q. Tian, X. Gu, L. Zhang, S. Zhang, K. Zhao and S. Liu, *Adv. Funct. Mater.*, 2021, **31**, 2101568.

85 X. Wang, X. Ran, X. Liu, H. Gu, S. Zuo, W. Hui, H. Lu, B. Sun, X. Gao, J. Zhang, Y. Xia, Y. Chen and W. Huang, *Angew. Chem., Int. Ed.*, 2020, **59**, 13354.

86 J. Zhang, Z. Wang, A. Mishra, M. Yu, M. Shasti, W. Tress, D. J. Kubicki, C. E. Avalos, H. Lu, Y. Liu, B. I. Carlsen, A. Agarwalla, Z. Wang, W. Xiang, L. Emsley, Z. Zhang, M. Grätzel, W. Guo and A. Hagfeldt, *Joule*, 2020, **4**, 222.

87 H. Zhao, Y. Fu, Z. Li, S. Yang, B. Xu, X. Liu, J. Xu, S. Frank Liu and J. Yao, *J. Mater. Chem. A*, 2021, **9**, 4922.

88 X. Gu, W. Xiang, Q. Tian and S. Frank Liu, *Angew. Chem.*, 2021, **133**, 23348.

89 W. Chen, D. Li, X. Chen, H. Chen, S. Liu, H. Yang, X. Li, Y. Shen, X. Ou, Y. Yang, L. Jiang, Y. Li and Y. Li, *Adv. Funct. Mater.*, 2022, **32**, 2109321.

90 J. Wang, J. Zhang, Y. Zhou, H. Liu, Q. Xue, X. Li, C. C. Chueh, H. L. Yip, Z. Zhu and A. K. Y. Jen, *Nat. Commun.*, 2020, **11**, 177.

91 W. Zhang, J. Xiong, J. Li and W. A. Daoud, *Adv. Energy Mater.*, 2021, **11**, 2003585.

92 Y. Zhao, K. Zhao, L. Wan, Y. Tan and Z. S. Wang, *ACS Appl. Mater. Interfaces*, 2022, **14**, 6906.

93 L. Ye, H. Wang, Y. Wei, P. Guo, X. Yang, Q. Ye and H. Wang, *ACS Appl. Energy Mater.*, 2020, **3**, 658.

94 Z. Zeng, J. Zhang, X. Gan, H. Sun, M. Shang, D. Hou, C. Lu, R. Chen, Y. Zhu and L. Han, *Adv. Energy Mater.*, 2018, **8**, 1801050.

95 I. S. Jin, K. S. Kim and J. W. Jung, *J. Power Sources*, 2021, **512**, 230481.

96 J. He, J. Liu, Y. Hou, Y. Wang, S. Yang and H. G. Yang, *Nat. Commun.*, 2020, **11**, 4237.

97 H. Li, X. Hao, B. Chang, Z. Li, L. Wang, L. Pan, X. Chen and L. Yin, *ACS Appl. Mater. Interfaces*, 2021, **13**, 40489.

98 C. F. J. Lau, X. Deng, Q. Ma, J. Zheng, J. S. Yun, M. A. Green, S. Huang and A. W. Y. Ho-Baillie, *ACS Energy Lett.*, 2016, **1**, 573.

99 W. Li, M. U. Rothmann, A. Liu, Z. Wang, Y. Zhang, A. R. Pascoe, J. Lu, L. Jiang, Y. Chen, F. Huang, Y. Peng, Q. Bao, J. Etheridge, U. Bach and Y. B. Cheng, *Adv. Energy Mater.*, 2017, 1700946.

100 B. Yang, M. Wang, X. Hu, T. Zhou and Z. Zang, *Nano Energy*, 2019, **57**, 718.

101 C. Liu, W. Li, J. Chen, J. Fan, Y. Mai and R. E. I. Schropp, *Nano Energy*, 2017, **41**, 75.

102 N. Li, Z. Zhu, J. Li, A. K. Y. Jen and L. Wang, *Adv. Energy Mater.*, 2018, 1800525.

103 W. Zhu, Q. Zhang, C. Zhang, Z. Zhang, D. Chen, Z. Lin, J. Chang, J. Zhang and Y. Hao, *ACS Appl. Energy Mater.*, 2018, **1**, 4991.

104 W. Zhang, J. Xiong, J. Li and W. A. Daoud, *Small*, 2020, **16**, 2001535.

105 C. Zhang, K. Wang, Y. Wang, W. S. Subhani, X. Jiang, S. Wang, H. Bao, L. Liu, L. Wan and S. Liu, *Sol. RRL*, 2020, **4**, 2000254.

106 H. Wang, S. Cao, B. Yang, H. Li, M. Wang, X. Hu, K. Sun and Z. Zang, *Sol. RRL*, 2020, **4**, 1900363.

107 H. Wang, H. Li, S. Cao, M. Wang, J. Chen and Z. Zang, *Sol. RRL*, 2020, **4**, 2000226.

108 A. K. Jena, A. Kulkarni, Y. Sanehira, M. Ikegami and T. Miyasaka, *Chem. Mater.*, 2018, **30**, 6668.

109 F. Ünlü, E. Jung, J. Haddad, A. Kulkarni, S. Öz, H. Choi, T. Fischer, S. Chakraborty, T. Kirchartz and S. Mathur, *APL Mater.*, 2020, **8**, 070901.

110 J. Liang, P. Zhao, C. Wang, Y. Wang, Y. Hu, G. Zhu, L. Ma, J. Liu and Z. Jin, *J. Am. Chem. Soc.*, 2017, **139**, 14009.

111 J. Liang, Z. Liu, L. Qiu, Z. Hawash, L. Meng, Z. Wu, Y. Jiang, L. K. Ono and Y. Qi, *Adv. Energy Mater.*, 2018, **8**, 1800504.

112 X. Tan, X. Liu, Z. Liu, B. Sun, J. Li, S. Xi, T. Shi, Z. Tang and G. Liao, *Appl. Surf. Sci.*, 2019, 143990.

113 Y. Guo, F. Zhao, Z. Li, J. Tao, D. Zheng, J. Jiang and J. Chu, *Org. Electron.*, 2020, **83**, 105731.

114 Y. Guo, F. Zhao, X. Wang, J. Tao, D. Zheng, J. Jiang, Z. Hu and J. Chu, *Sol. Energy Mater. Sol. Cells*, 2021, **221**, 110918.

115 H. Sun, L. Yu, H. Yuan, J. Zhang, X. Gan, Z. Hu and Y. Zhu, *Electrochim. Acta*, 2020, **349**, 136162.

116 P. Liu, X. Yang, Y. Chen, H. Xiang, W. Wang, R. Ran, W. Zhou and Z. Shao, *ACS Appl. Mater. Interfaces*, 2020, **12**, 23984.

117 Y. Long, C. Wang, X. Liu, J. Wang, S. Fu, J. Zhang, Z. Hu and Y. Zhu, *J. Mater. Chem. C*, 2021, **9**, 2145.

118 J. Lin, M. Lai, L. Dou, C. S. Kley, H. Chen, F. Peng, J. Sun, D. Lu, S. A. Hawks, C. Xie, F. Cui, A. P. Alivisatos, D. T. Limmer and P. Yang, *Nat. Mater.*, 2018, **17**, 261.

119 Y. Jiang, J. Yuan, Y. Ni, J. Yang, Y. Wang, T. Jiu, M. Yuan and J. Chen, *Joule*, 2018, **2**, 1356.

120 W. Zhang, H. Liu, X. Qi, Y. Yu, Y. Zhou, Y. Xia, J. Cui, Y. Shi, R. Chen and H. L. Wang, *Adv. Sci.*, 2022, 2106054.

121 D. Wang, W. Li, T. Zhang, X. Liu, X. Jin, B. Xu, D. Li, Z. Huang, Q. Li, Z. Lan and J. Wu, *ACS Appl. Energy Mater.*, 2022, **5**, 2720.

122 J. Huang, S. He, W. Zhang, A. Saparbaev, Y. Wang, Y. Gao, L. Shang, G. Dong, L. Nurumbetova, G. Yue and Y. Tu, *Sol. RRL*, 2022, **6**, 2100839.

123 J. Yang, H. Yu, S. Wu, C. Cai, J. Gao, X. Lu, X. Gao, L. Shui, S. Wu and J.-M. Liu, *ACS Appl. Energy Mater.*, 2022, **5**, 2881.

124 Z. Guo, A. K. Jena, I. Takei, G. M. Kim, M. A. Kamarudin, Y. Sanehira, A. Ishii, Y. Numata, S. Hayase and T. Miyasaka, *J. Am. Chem. Soc.*, 2020, **142**, 9725.

125 S. Oz, K. A. Jena, A. Kulkarni, K. Mouri, T. Yokoyama, I. Takei, F. Unlu, S. Mathur and T. Miyasaka, *ACS Energy Lett.*, 2020, **5**, 1292.

126 Z. Guo, A. K. Jena, I. Takei, M. Ikegami, A. Ishii, Y. Numata, N. Shibayama and T. Miyasaka, *Adv. Funct. Mater.*, 2021, **31**, 2103614.

127 H. Zhong, W. Li, Y. Huang, D. Cao, C. Zhang, H. Bao, Z. Guo, L. Wan, X. Zhang, X. Zhang, Y. Li, X. Ren, X. Wang, D. Eder, K. Wang, S. F. Liu and S. Wang, *ACS Appl. Mater. Interfaces*, 2022, **14**, 5183.

128 X. Zhao, T. Liu, Q. C. Burlingame, T. Liu, R. Holley, G. Cheng, N. Yao, F. Gao and Y. L. Loo, *Science*, 2022, **377**, 307.

129 W. S. Subhani, K. Wang, M. Du, X. Wang and S. Frank Liu, *Adv. Energy Mater.*, 2019, 1803785.

130 W. Zhu, Z. Zhang, W. Chai, Q. Zhang, D. Chen, Z. Lin, J. Chang, J. Zhang, C. Zhang and Y. Hao, *ChemSusChem*, 2019, **12**, 2318.

131 Z. Guo, S. Teo, Z. Xu, C. Zhang, Y. Kamata, S. Hayase and T. Ma, *J. Mater. Chem. A*, 2019, **7**, 1227.

132 J. Wang, X. Wu, Y. Liu, Q. Xue, H. L. Yip, A. K. Y. Jen and Z. Zhu, *Energy Technol.*, 2021, **9**, 2100562.

133 X. Jiang, W. S. Subhani, K. Wang, H. Wang, L. Duan, M. Du, S. Pang and S. Liu, *Adv. Mater. Interfaces*, 2021, **8**, 2001994.

134 J. Du, J. Duan, X. Yang, Y. Duan, Q. Zhou and Q. Tang, *Angew. Chem., Int. Ed.*, 2021, **60**, 10608.

135 D. Wang, W. Li, R. Li, W. Sun, J. Wu and Z. Lan, *Sol. RRL*, 2021, **5**, 2100375.

136 Y. Xu, Q. Wang, L. Zhang, M. Lyu, H. Lu, T. Bai, F. Liu, M. Wang and J. Zhu, *Sol. RRL*, 2021, **5**, 2100669.

137 J. Lu, S. C. Chen and Q. Zheng, *ACS Appl. Energy Mater.*, 2018, **1**, 5872.

138 Y. You, W. Tian, M. Wang, F. Cao, H. Sun and L. Li, *Adv. Mater. Interfaces*, 2020, **7**, 2000537.

139 J. Pan, X. Zhang, Y. Zheng and W. Xiang, *Sol. Energy Mater. Sol. Cells*, 2021, **221**, 110878.

140 Y. Wang, K. Wang, W. S. Subhani, C. Zhang, X. Jiang, S. Wang, H. Bao, L. Liu, L. Wan and S. Liu, *Small*, 2020, **16**, 1907283.

141 W. Zhu, Q. Zhang, D. Chen, Z. Zhang, Z. Lin, J. Chang, J. Zhang, C. Zhang and Y. Hao, *Adv. Energy Mater.*, 2018, **8**, 1802080.

142 Q. Zhang, W. Zhu, D. Chen, Z. Zhang, Z. Lin, J. Chang, J. Zhang, C. Zhang and Y. Hao, *ACS Appl. Mater. Interfaces*, 2019, **11**, 2997.

143 B. Zhang, W. Bi, Y. Wu, C. Chen, H. Li, Z. Song, Q. Dai, L. Xu and H. Song, *ACS Appl. Mater. Interfaces*, 2019, **11**, 33868.

144 Y. Guo, X. Yin, J. Liu and W. Que, *J. Mater. Chem. A*, 2019, **7**, 19008.

145 X. Jiang, K. Wang, H. Wang, L. Duan, M. Du, L. Wang, Y. Cao, L. Liu, S. Pang and S. Frank Liu, *Small Sci.*, 2021, **1**, 2000054.

146 Q. Zhang, J. Duan, Q. Guo, J. Zhang, D. Zheng, F. Yi, X. Yang, Y. Duan and Q. Tang, *Angew. Chem.*, 2022, **134**, e202116632.

147 F. Yan, P. Yang, J. Li, Q. Guo, Q. Zhang, J. Zhang, Y. Duan, J. Duan and Q. Tang, *Chem. Eng. J.*, 2022, **430**, 132781.

148 Q. Wang, Y. Xu, L. Zhang, A. Yang, T. Bai, F. Liu, M. Lyu and J. Zhu, *ACS Appl. Energy Mater.*, 2022, **5**, 3110.